PREDICTION OF AUTOMOTIVE TURBOCHARGER NONLINEAR DYNAMIC FORCED RESPONSE WITH ENGINE-INDUCED HOUSING EXCITATIONS: COMPARISONS TO TEST DATA

A Thesis

by

ASHLEY MARUYAMA

Submitted to the Office of Graduate Studies of
Texas A&M University
in partial fulfillment of the requirements for the degree of

MASTER OF SCIENCE

December 2007

Major Subject: Mechanical Engineering

PREDICTION OF AUTOMOTIVE TURBOCHARGER NONLINEAR DYNAMIC FORCED RESPONSE WITH ENGINE-INDUCED HOUSING EXCITATIONS: COMPARISONS TO TEST DATA

A Thesis

by

ASHLEY MARUYAMA

Submitted to the Office of Graduate Studies of
Texas A&M University
in partial fulfillment of the requirements for the degree of

MASTER OF SCIENCE

Approved by:

Chair of Committee, Luis San Andrés
Committee Members, Dara Childs
Mark Holtzapple
Head of Department, Dennis L. O'Neal

December 2007

Major Subject: Mechanical Engineering

ABSTRACT

Prediction of Automotive Turbocharger Nonlinear Dynamic Forced Response With Engine-Induced Housing Excitations: Comparisons to Test Data. (December 2007)

Ashley Maruyama, B.S., Texas A&M University

Chair of Advisory Committee: Dr. Luis San Andrés

The trend in passenger vehicle internal combustion (IC) engines is to produce smaller, more fuel-efficient engines with power outputs comparable to those of large displacement engines. One way to accomplish this goal is through using turbochargers (TCs) supported on semi-floating ring bearings (SFRBs). The thesis presents progress on the nonlinear modeling of rotor-bearing systems (RBSs) by including engine-induced TC housing excitations. Test data collected from an engine-mounted TC unit operating to a top speed of 160 krpm (engine speed = 3,600 rpm) validates the nonlinear predictions of shaft motion. Engine-induced housing excitations are input into the nonlinear time transient rotor model as Fourier coefficients (and corresponding phase angles) derived from measured TC center housing accelerations.

Analysis of recorded housing accelerations shows the IC engine induces TC motions with a broad range of subsynchronous frequencies, rich in engine (*e*) super-harmonics. In particular, *2e* and *4e* vibration frequencies contribute greatly to housing motion. Most importantly, the analysis reveals TC center and compressor housings do *not* vibrate as a rigid body.

Eigenvalue analysis of the TC system evidences four damped natural frequencies within the TC operating speed range. However, only the highest damped natural frequency (first elastic mode, f = 2,025 Hz, ξ = 0.14) is lightly-damped (critical speed = 150 krpm). Predicted linear and nonlinear imbalance response amplitudes increase with TC shaft speed, with linear predictions agreeing with test data at high shaft speeds. The differences between predictions and test data are attributed to an inaccurate knowledge of the actual TC rotor imbalance distribution.

For the nonlinear analysis, predicted shaft motions not accounting for housing accelerations show the TC is stable (i.e. no subsynchronous whirl) at all but the lowest shaft speeds (<70 krpm). However, predicted shaft motions accounting for housing accelerations, as well as the test data, reveal TC motions rich in subsynchronous activity. Clearly, engine-induced housing accelerations have a significant impact on TC shaft motions. Predicted total shaft motions show good agreement with test data. Predicted nonlinear subsynchronous amplitudes as well as peak shaft amplitudes also agree well with test data. However, nonlinear predictions only show TC shaft vibrations attributed to engine order frequencies below *6e*, whereas test data evidences TC vibrations are due to order frequencies greater than *6e*. Overall, nonlinear predictions and test data illustrate the importance of accounting for engine-induced housing vibrations in the design and operation of TC systems. The good agreement between predictions and test data serve to validate the rotor model. The tools developed will aid a TC manufacturer in reducing development time and expenditures.

DEDICATION

This thesis is dedicated to

My father and mother, for their unconditional love and support

My grandmother, for her unwavering confidence in me

My closest and best friend, Mike Jordhoy, for his invaluable friendship through thick and thin

My late grandfather, I hope I have made you proud

ACKNOWLEDGEMENTS

First and foremost, I would like to thank my advisor, Dr. Luis San Andrés, who gave me the opportunity to pursue my goals. His guidance, support, and patience are invaluable.

I would like to thank my thesis committee members, Dr. Dara Childs, and Dr. Mark Holtzapple, for taking time to give advice and input.

I also thank my sponsor, Honeywell Turbo Technologies, for supporting my research.

I must also thank all my colleagues and friends at the Turbomachinery Laboratory for their help, support, and friendship: Adolfo Delgado, Anthony Breedlove, Jose Baker, Keun Ryu, Tae Ho Kim, Chad Jarrett, Arian Vistamehr, Michael Forsberg, Fernando Ramirez, Joel Harris, Vinayaka Rajagopalan. I especially wish to thank Adolfo Delgado and Keun Ryu for their help and advice; research would have been extremely rough without them. I would also like to thank Mr. Eddie Denk for his assistance.

I would like to thank my fellow colleague, Brandon Gegg. I would not be here if it was not for his expertise and willingness to share his knowledge.

Finally, I would like to thank my girlfriend, Vanna Keller, for all her love, encouragement, and understanding. They mean more to me than words can express.

NOMENCLATURE

a	Acceleration
A	Magnitude of engine frequency
A_0	Magnitude of zero order frequency
C	Bearing radial clearance
$e, 2e, \ldots$	Fundamental engine frequency, 2 times fundamental engine frequency, . . .
F	Damped natural frequency
n	Order of fundamental engine frequency
N_F	Maximum order of the fundamental engine frequency
R	Floating ring radius
t	Time
T	Turbocharger shaft temperature
x	Horizontal axis of turbocharger shaft motion
y	Vertical axis of turbocharger shaft motion
φ	Phase of engine frequency
θ	Defect temperature ratio
ω_e	Fundamental engine frequency
ξ	Damping ratio

Subscripts

i	Inner
j	Measurement location along turbocharger shaft
n	Order of fundamental engine frequency
o	Outer

TABLE OF CONTENTS

Page

Page

LIST OF FIGURES

Page

Page

Page

LIST OF TABLES

Page

I INTRODUCTION

The trend in passenger vehicle internal combustion (IC) engines is to produce smaller, more fuel-efficient engines with power outputs comparable to those of large displacement engines. One way to accomplish this goal is through using turbochargers. In a turbocharger (TC), exhaust gases drive a turbine wheel which is connected to a compressor wheel by a thin shaft. The compressor forces a denser charge of air (i.e. larger air mass) into the engine cylinders, allowing more fuel to be added, thus producing more power. While simple in concept, TC design and operation are complex. Figure 1 shows an assembly cut of a typical TC.

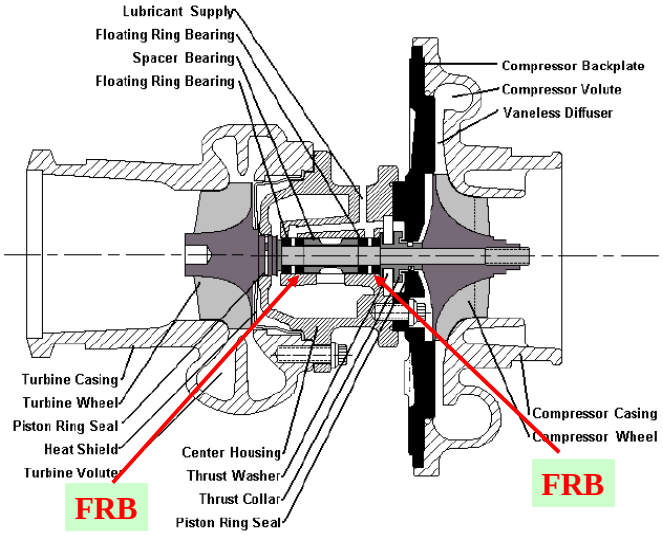

Figure 1. Assembly cut of a typical TC. Taken from Ref. [1]

As a TC rotor spins, it vibrates due to several causes (imbalance, engine-induced vibrations, aerodynamic loading, pressure fluctuations, etc.). The vibration amplitudes need to be controlled to ensure TC reliability. Bearings greatly affect TC performance, and are a key feature of a reliable TC design. TCs are usually supported by one of three bearing types: ball bearings, floating-ring bearings (FRB), or semi-floating-ring bearings (SFRB) (see Figure 2).

This thesis follows the style of Transactions of the ASME.

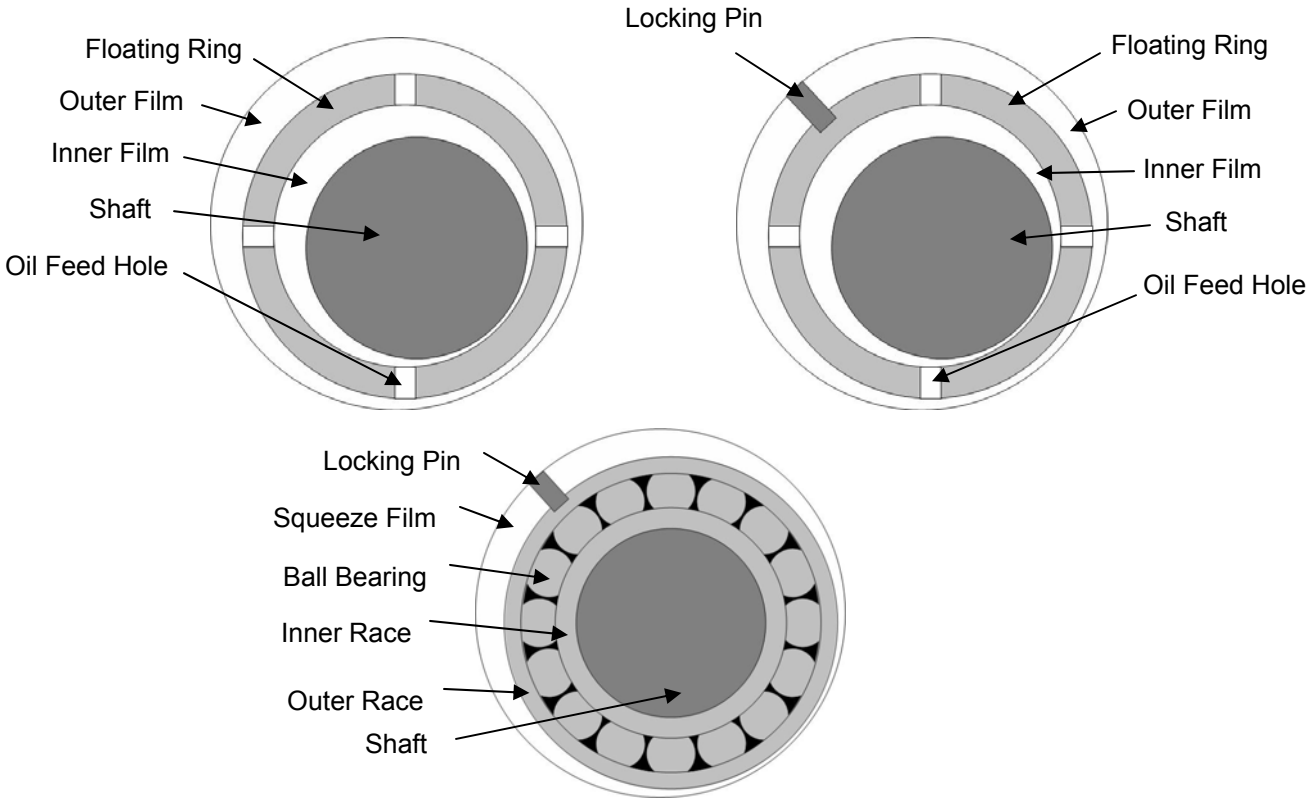

Figure 2. Schematic view of floating ring, semi-floating ring, and ball-type bearings

FRBs consist of a floating ring loosely fitted within the shaft and TC housing, thereby creating two oil films (inner and outer) in series. The ring is free to rotate and precess, and spins at a fraction of the shaft speed due to viscous drag shear from the inner and outer films. SFRBs are similar in geometry to FRBs; however, the ring is prevented from rotating by a locking pin (or button). Thus, the outer film acts solely as a squeeze-film damper. Ball bearings are usually backed by a squeeze-film damper (refer to Figure 2).

While ball bearings yield the smallest TC shaft vibration amplitudes [2], they have a limited lifespan. FRBs and SFRBs are more economic, although like ball bearings, must be designed and lubricated properly to limit shaft vibration amplitudes [2]. Traditionally, TC development consists of costly gas test stand iteration. Present research focuses on the development of fast and accurate computational tools to accurately predict TC shaft motions, reducing (or eliminating) the need for repetitive test stand certification and qualification.

II LITERATURE REVIEW

A floating-ring bearing (FRB) consists of a ring inserted between a journal and its bearing housing, thereby forming two fluid films in series. The ring is free to rotate, or fixed if semi-floating ring bearing (SFRB). Fluid flow shear in the inner film drives ring rotation, while shear in the outer film retards its rotation. Therefore, the ring is subjected to two opposing torques and spins at a fraction of shaft speed. FRBs (and SFRBs) offer decreased power losses, lower operating temperatures, and superior stability compared to conventional cylindrical journal bearings [3-7]. However, accurate prediction of FRB and TC (supported on FRBs) dynamic forced response has proven difficult since the system is highly nonlinear.

In [4], Tatara conducts experiments to determine the stability characteristics of a rotor supported on FRBs. A test rotor is operated to a maximum speed of 70 krpm with FRBs of various inner and outer clearances. Test results show that the rotor initially unstable operation becomes stable at high shaft speeds, lending credibility to the concept of a FRB superior stability over plain journal bearings. However, the ring speed reaches a nearly constant magnitude at shaft speeds greater than 10 krpm. This result is contrary to the familiar knowledge that the ring speed increases with shaft speed.

In an effort to explain this unusual behavior, Trippett and Li [8] compare test data to predictions derived with isothermal and thermal bearing flow analyses (lubricant viscosity and clearances varying with temperature). Test data show the ring reaches a nearly constant speed as shaft speed increases. Isothermal model predictions, however, show a linear increase in ring speed. Only the thermal model results show good correlation with ring speed test data. Clearly, an isothermal bearing analysis is unsuitable for FRBs. A more comprehensive thermal analysis is needed to accurately model FRBs.

Experimental and numerical analyses of TCs supported on FRBs also show TC stability depends greatly on FRB geometry. Tanaka and Hori [9] present a stability analysis of a short length rigid rotor supported on FRBs. Cavitation of the oil film is assumed to occur in the region where the film pressure becomes nil. Stability charts for various bearing outer (C_o) to inner clearance (C_i) ratios ($0.8 \le C_o/C_i \le 4.0$) and floating ring outer (R_o) to inner (R_i) radius ratios ($1.20 \le R_o/R_i \le 1.44$) show that the TC stable

operating speed region increases as the clearance ratio and radii ratio increase. The stability analysis also shows that the rotor system can traverse several regions of stable and unstable behavior, in agreement with experimental results in Ref. [4]. Also presented in Ref. [9] are experimental results for a rotor operating with FRBs supplied with oil at various feed pressures. Two subsynchronous frequencies of rotor motion are observed depending on the feed pressure. At higher supply pressures, a frequency approximately equal to half of the ring speed is observed. At lower supply pressures, a frequency of approximately half of the ring plus journal speeds appears. In Ref. [7], Li confirms these findings theoretically and attributes the "half frequency whirl" to instabilities in the outer and inner films, respectively.

Li and Rohde [6] perform an analysis of the steady state and dynamic force performance characteristics of a FRB utilizing a linear stability analysis and numerical integration to solve the equations of motion of a rotor-FRB system. Interestingly, the nonlinear analysis shows the rotor-FRB system reaches stable limit cycles, regardless of the initial conditions used. Moreover, stable limit cycles with subsynchronous frequencies occur even outside the predicted linear stability range. The authors caution, however, that the bearing outer film to inner film clearance ratio must be carefully chosen to allow for such operation. Li [7] expands on the analysis in Ref. [6] identifying three major types of rotor frequency response: half ring speed frequency (instability in the outer film), half ring-plus-journal speeds frequency (instability in the inner film), and synchronous frequency (response to imbalance). The ring speed increases with decreasing inner film clearance and decreases with decreasing outer film clearance. Similarly, power consumption decreases with increasing inner film clearance and is relatively unaffected by changes in the outer film clearance. These results are in agreement with previous numerical results obtained by Rohde and Ezzat [5].

Holmes [10] presents a numerical analysis of a TC supported on FRBs using eigenvalues to characterize subsynchronous frequencies observed experimentally. The analysis predicts two subsynchronous frequencies, agreeing qualitatively with test results. Moreover, the analysis also correctly shows that the dominance of each subsynchronous frequency is a function of rotor speed and that the change in the dominant subsynchronous frequency occurs suddenly.

The increase in computer computational power allows for experimental and numerical analyses to focus on predicting TC shaft motion nonlinear dynamic response, rather than only rotor linear stability or bearing characteristics. In 2003, Holt et al. [11] present measurements of housing acceleration on an automotive turbocharger (TC) supported on FRBs. The turbine is driven by pressurized air at ambient temperatures to a top speed of 115 krpm. Lubricant feed temperature and pressure are varied to determine their effect on system rotordynamic response. Test data waterfalls show two subsynchronous frequencies which track the rotor speed, indicating a condition of oil-whirl. Surprisingly, no subsynchronous motions exist above 90 krpm. Lubricant feed temperature shows minimal effect on the onset and end speeds of instabilities, whereas increasing feed pressure tends to delay the onset of an instability. In a companion paper, Holt et al. [12] present linear and nonlinear rotordynamic models to predict TC forced response and compare the predictions to test data given in [11]. The linear model uses linearized bearing force coefficients and predicts well the onset speed of instability. The nonlinear model relies on numerical integration of the equations of motion while incorporating instantaneous bearing reaction forces, predicting limit cycle orbits with two subsynchronous frequencies of approximately 50% of ring speed and 50% of ring plus journal speeds. The nonlinear model also demonstrates the importance of rotor imbalance in ameliorating subsynchronous motion amplitudes at high speeds. This behavior is evidenced by test data and predictions using an assumed imbalance but not by predictions without mass imbalance.

San Andrés and Kerth [13] extend the previous model in [12] by incorporating a thermo-hydrodynamic flow model to predict FRB forced response. The model includes a lumped-parameter thermal energy balance to estimate the lubricant viscosity and changes in clearances due to thermal growth of the journal, ring, and bearing. Ring speed predictions show fair estimation of actual test data, displaying the same decreasing trend, albeit at a lower rate than test data indicates. The authors note that static bearing load values are unknown due to aerodynamic forces caused by the compressor and turbine. Predictions of power losses show good correlation with test data at low speeds (< 35 krpm) but slightly under predict values at high speeds (> 55 krpm, 65 krpm max.). The novel FRB model is also fully integrated into a finite element-based (FE) rotordynamics

model, which predicts well the frequency content of the rotor response but tends to over predict rotor motion amplitudes. However, the actual imbalance distribution of the test TC is unknown and could explain the discrepancies between predictions and test data.

San Andrés et al. [14] continue to refine the FRB flow model and present comparisons of predictions to test data of a TC supported on a semi-floating ring bearing (SFRB). In a SFRB, a locking pin or button allows the ring to precess but not rotate. The bearing flow model is updated to include calculated hydrostatic (side) loads due to external pressurization. The nonlinear predictions presented are taken from the last 1024 time steps of numerical integration of the equations of motion, thereby capturing a quasi steady-state motion of the TC. Subsequent Fast Fourier Transformations (FFTs) of the time responses reveal shaft motions rich in subsynchronous activity. Predictions reveal large subsynchronous vibrations throughout the TC speed range (29.7 krpm – 244 krpm) at an oil feed pressure of 4 bar. Subsynchronous amplitudes and frequencies correlate well with test data. Predicted total motions at the compressor end, calculated as the maximum whirl orbit at a given shaft speed, are generally over predicted. However, predictions are well below the physical limit, which still serves to lend credibility to the analysis. Nonlinear predictions of the synchronous response to imbalance agree well with test data over the entire speed range. Discrepancies between the two are attributed to uncertainty in the imbalance distribution of the actual TC. Predicted whirl frequency ratios (WFRs) of the subsynchronous vibrations are also presented and correlate well with test data, though a third, higher WFR is predicted but not evidenced by the test data. Test data (and predictions) indicate that the WFRs tend to coincide with the rotor conical mode of vibration and its harmonics.

Rivadeneira [15] presents a comprehensive investigation of shaft motions of a FRB-supported TC, detailing comparisons of test data to predictions based on the models developed in Refs. [12-14]. Ref. [16] presents a summary of the same results. The FRB model presented in [13] is updated to include centrifugal pressure losses into the inner film. These losses arise from fluid rotation forcing the lubricant out of the bearing. The fluid rotation also leads to increased lubricant residence time in the bearing, which increases resistance to fluid flow. After validating the rotor model against free-free mode tests, the author presents results of a linear eigenvalue analysis. Three critical speeds are

predicted at 4, 20, and 67.5 krpm corresponding with the conical, cylindrical, and first elastic bending modes of the rotor, respectively.

A method to estimate rotor imbalance distribution using influence coefficients (detailed in Ref. [15]) is used to reflect more accurately the actual rotor imbalance distribution. Synchronous response predictions show good correlation to test data, especially at low and high shaft speeds. Nonlinear predictions show that subsynchronous amplitudes and frequencies are predicted well; however, the predictions show an absence of subsynchronous activity above 55 krpm. On the other hand, test data displays subsynchronous vibrations throughout the operating speed range. Predicted total shaft motions show excellent correlation with test data, especially at shaft speeds above 25 krpm.

Recent work conducted by Gjika and Groves [17] compares test data to predictions for a TC supported on FRBs. The predictive model used is based on that developed in Refs. [12-14]. Both the nonlinear analysis and test results show large subsynchronous vibrations throughout the TC operating speed range. The predicted subsynchronous frequency content also agrees well with test data. While predicted subsynchronous amplitudes are smaller than test results indicate, both are larger than synchronous amplitudes. Due to the discrepancy in subsynchronous amplitudes, predicted total motion amplitudes are less than test results, but still show the same general decreasing (with rotor speed) trend. Currently, the nonlinear rotordynamics model aids the development of TC rotor-bearing systems (RBS) at a well-known TC manufacturer.

Predicted TC rotor motion is most often compared to test data obtained in test stands. In this setup, the TC housing is not subjected to any external loading. However, automotive TCs are subjected to a wide range of engine vibrations that can drastically affect TC response. Sahay and LaRue [2] present a comparison of recorded total shaft motion for identical automotive TCs mounted on a test stand and on an internal combustion (IC) engine. As noted by the authors, engine vibrations (and pulsed loading on the turbine) cause TC shaft motion amplitudes to be typically 20% – 30% larger than those recorded in a test stand. Recently, Kirk et al. [18] perform shaft motion measurements of an automotive FRB-supported TC mounted on a 3.9L 4-cylinder diesel

engine. Waterfalls of shaft motion clearly show two subsynchronous frequencies and several lower frequencies vibrations attributed to engine vibration. Interestingly, with no load placed on the engine, engine induced vibration amplitudes are much smaller than those caused by TC subsynchronous motions. However, at full engine load, engine induced vibrations become comparable in magnitude to TC shaft vibrations, demonstrating the dramatic effect engine motion and engine loading condition can have on TC response. Unfortunately, no comparison of the total TC motion from each test is made.

Other studies also show that the frequency of external vibration affects TC response. Hori and Kato [19] present a numerical analysis of a Jeffcott rotor supported on plain oil-film journal bearings subjected to external shocks. Eigenvalue analysis indicates the otherwise stable rotor can become unstable at speeds above twice the critical speed due to sufficiently large external shocks. In addition, unstable operation results when the external shock frequency is close to that of the natural frequency of the RBS. Lee et al. [20] also demonstrate both analytically and experimentally that vibration amplitudes are amplified when the external shock frequency is close to a system natural frequency.

This thesis presents progress on the refinement of the linear and nonlinear rotordynamic models developed in [12-14] in predicting the response of a TC supported on a SFRB. San Andrés [21] has updated the bearing model to include centrifugal pressure losses into the inner film and the inclusion of non-cylindrical lubricant films in the calculation of SFRB stiffness and damping force coefficients. The nonlinear model can predict TC response with specified base excitations (to simulate engine vibrations).

III TURBOCHARGER STRUCTURAL FINITE ELEMENT MODEL AND SEMI-FLOATING RING BEARING (SFRB) THERMAL MODEL

Turbocharger Rotor-Bearing System Finite Element Modeling

Figure 3 displays the GT1749 TC rotor assembly (SFRB and thrust bearing unavailable for photography). At the sponsor request, all RBS physical properties (dimensions, geometry, imbalances, etc.) are not presented. The SFRB is a one-piece design integrating the compressor and turbine bearing ends. A button pin prevents ring rotation (bearing and bearing model to be discussed in depth later).

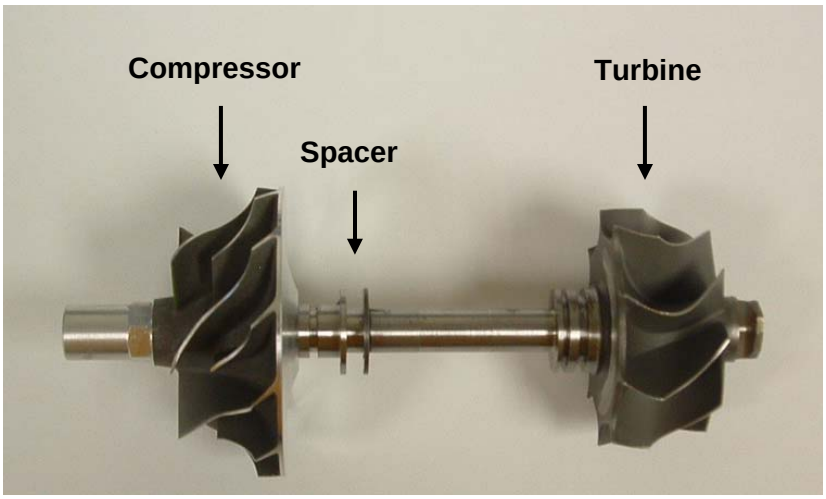

Figure 3. GT1749 TC rotor assembly

Figure 4 shows the TC rotordynamic model, constructed using an in-house rotordynamics software, XLTRC^2 [22]. The model consists of 43 finite elements (44 stations) for the rotor, including the thrust collar and spacer, and 13 finite elements (stations 45-58) for the SFRB. Complicated geometrical parts, such as the compressor and turbine wheels, are modeled as low-density sections with added mass properties. The spring-connections represent a fluid film bearing. Note that only outer film connections are visible. Inner film connections are present but are too small to be distinguishable.

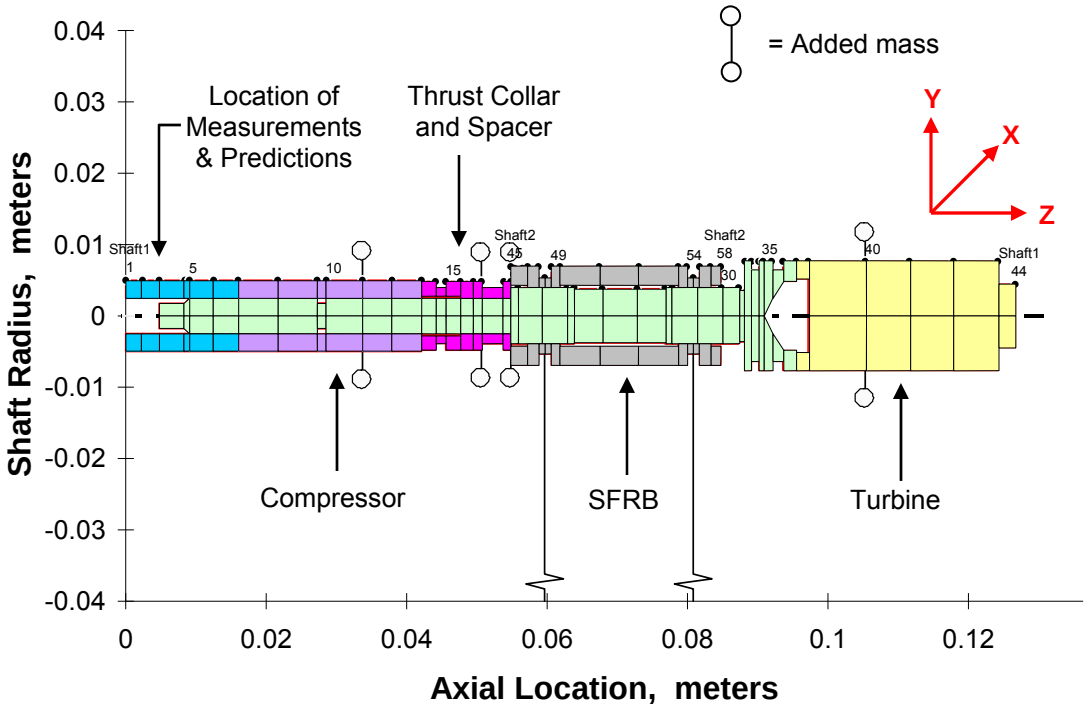

Figure 4. GT1749 rotordynamics FE model

The rotordynamics model uses an imbalance mass distribution in four planes as specified by the TC manufacturer. However, the imbalance distribution is only an estimation and may not accurately reflect the actual imbalance of the TC used during testing.

Validation of the rotordynamics model requires good correlation between measured and predicted rotor physical properties, as well as free-free natural frequencies and mode shapes. This step is essential for proving the accuracy of the rotor structural model. Again, rotor physical properties are not presented at the sponsor request. Nonetheless, agreement between measured and predicted values is excellent.

To measure the natural frequencies and mode shapes, the rotor is suspended from long wires so as to provide negligible stiffness in the horizontal plane. Two 0.2-gram piezoelectric accelerometers, one reference and one roaming, are used to measure the natural frequencies and trace the corresponding mode shapes. The rotor is excited with a small screwdriver and the results are considered valid if the phase angle difference between the two accelerometers is approximately 0° or ±180°. A total of five measurements are recorded at each location for the first and second natural frequencies and averaged to determine the final accepted value. The instrumentation used includes:

- Spectrum Analyzer HP Dynamic Signal Analyzer, Agilent Model 35670A
- PCB 0.2-gram Accelerometer, Model: 352C23, Sensitivity: 4.316 mV/g
- PCB Power Supply, Model: 482A16 Serial: 2767

Table 1 compares the measured and predicted free-free natural frequencies. The predicted frequencies agree well with the test data, thus validating the rotor model. Figure 5 and Figure 6 overlay on the rotor geometry the measured and predicted mode shapes corresponding to the first and second natural frequencies, respectively. The first predicted mode shape shows excellent correlation with test data. The second predicted mode shape also correlates well with test data, although measurements show slightly larger displacements at ~0.045 m (thrust collar) and ~0.085 m (turbine wheel back-face) axial locations. Still, the good correlation of both mode shapes validates the rotor model.

Table 1. Comparison of measured and predicted free-free natural frequencies

	Measured [kHz]	**Predicted** [kHz]	**% difference** -
First Freq.	1.799	1.823	**1.32**
Second Freq.	4.938	4.559	**7.67**

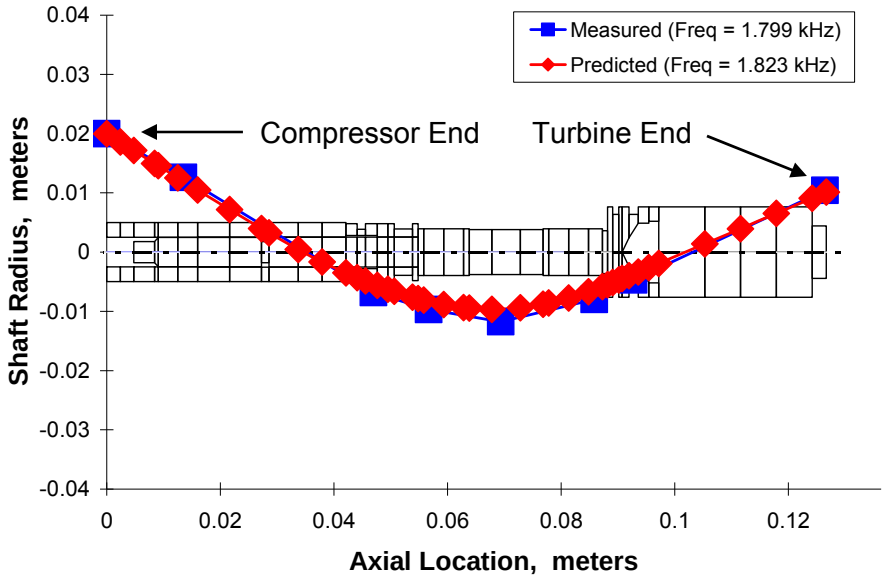

Figure 5. Measured and predicted first free-free natural frequency mode shapes

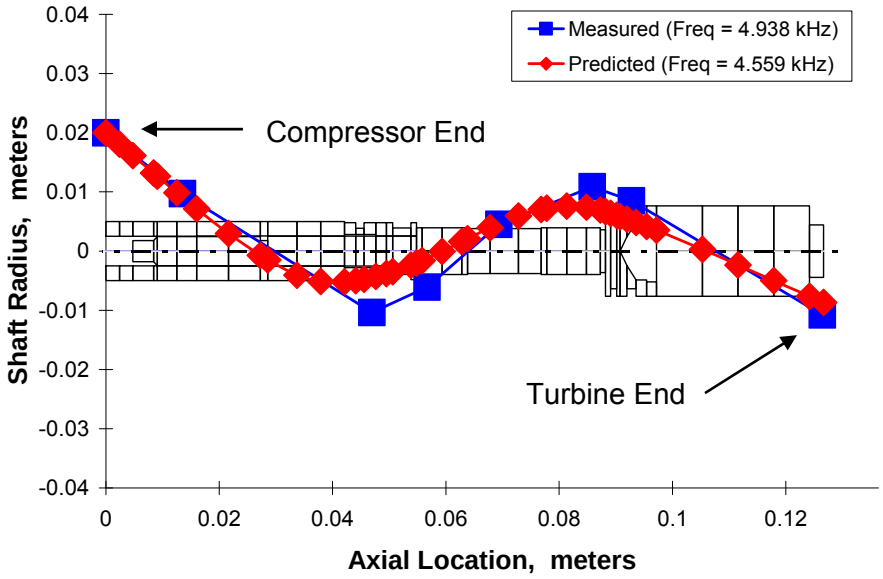

Figure 6. Measured and predicted second free-free natural frequency mode shapes

Semi-Floating Ring Bearing Model

The SFRB is modeled using an updated version of the bearing thermal flow model (XLFEMSFRB™ version 6 [23]) advanced in Refs. [13,15]. The model calculates bearing static performance parameters, incorporating a thermo-hydrodynamics fluid flow model predicting bearing forced response. The model includes a lumped-parameter

thermal energy balance to estimate the lubricant viscosity and changes in clearances due to thermal growth of the shaft (journal), ring, and bearing, as well as hydrostatic (side) loads due to external pressurization. Ref. [15] gives a detailed description of the computational model [24] to estimate side loads.

The GT1749 bearing housing incorporates a half-moon groove at the turbine bearing end and an anti-rotation button pin at the compressor bearing end. Along with bearing geometry, the computational analysis requires as input TC shaft speeds, oil inlet conditions, hydrostatic side loads, centrifugal pressure loss factors, bearing material properties, and shaft, housing, and ring temperatures.

Test data for the GT1749 TC was collected by the TC manufacturer, Ref. [25], on an IC engine test stand at three engine loads: 25%, 50%, and 100% of full engine load. Table 2 lists the engine speed, TC speed, bearing oil supply pressure, bearing oil supply temperature, and estimated compressor and turbine hydrostatic side loads for each engine load condition.

One must be cautious when using oil supply pressure data. Recent test data reported in Ref. [26] evidence a significant pressure drop from the TC upstream supply pipe into the bearing outer film. Thus, an inlet pressure loss factor, defined as the ratio of the bearing outer film pressure to the upstream recorded oil inlet pressure, is implemented to account for the pressure drop. Measurements by the TC manufacturer show the GT1749 inlet pressure loss factor is 0.835 for the compressor side and 0.71 for the turbine side [26]. Subsequently, all oil supply pressures input into the bearing model are reduced by their respective factors. However, hydrostatic side loads, while dependent on supply pressure, are calculated using the original supply pressures due to pressure stagnation at the ring outer surface.

Table 2. SFRB test conditions and estimated bearing hydrostatic side loads

25% Engine Load

Engine Speed [rpm]	TC Speed [rpm]	Oil Supply Pressure [bar]	Oil Supply Temperature [°C]	Compressor Bearing Side Load [N]	Turbine Bearing Side Load [N]
1,000	35,634	1.3	100.7	-4.25	-8.80
1,250	46,212	1.8	96.8	-5.80	-11.80
1,750	71,712	2.3	104.7	-7.47	-15.13
2,000	83,148	2.5	106.8	-8.20	-16.60
2,250	95,718	2.7	109.6	-8.71	-17.68
2,500	108,888	2.8	112.7	-9.02	-18.37
2,750	119,976	2.9	114.5	-9.40	-19.17
3,000	130,068	2.9	117.7	-9.41	-19.27
3,250	139,494	2.9	121.3	-9.15	-18.82
3,600	145,260	2.8	124.5	-9.06	-18.68

50% Engine Load

Engine Speed [rpm]	TC Speed [rpm]	Oil Supply Pressure [bar]	Oil Supply Temperature [°C]	Compressor Bearing Side Load [N]	Turbine Bearing Side Load [N]
1,000	39,558	1.3	98.4	-4.34	-8.98
1,250	53,136	1.8	96.3	-5.80	-11.82
1,750	85,584	2.3	104.7	-7.38	-15.02
2,000	99,774	2.5	106.7	-8.12	-16.55
2,250	113,118	2.7	109.4	-8.59	-17.55
2,500	125,862	2.8	112.4	-8.91	-18.26
2,750	136,170	2.9	114.5	-9.23	-18.96
3,000	141,912	2.9	117.7	-9.27	-19.06
3,250	145,308	2.9	121.0	-9.11	-18.77
3,600	149,430	2.8	124.4	-8.99	-18.55

100% Engine Load

Engine Speed [rpm]	TC Speed [rpm]	Oil Supply Pressure [bar]	Oil Supply Temperature [°C]	Compressor Bearing Side Load [N]	Turbine Bearing Side Load [N]
1,000	48,504	1.3	97.9	-4.34	-9.01
1,250	69,366	1.7	97.3	-5.67	-11.63
1,750	120,216	2.2	106.3	-7.06	-14.57
2,000	134,298	2.4	108.8	-7.62	-15.75
2,250	141,762	2.5	111.2	-8.07	-16.67
2,500	144,036	2.6	114.6	-8.42	-17.39
2,750	146,106	2.8	116.0	-8.84	-18.23
3,000	148,722	2.7	119.9	-8.77	-18.11
3,250	152,532	2.7	122.6	-8.71	-18.02
3,600	157,674	2.7	126.1	-8.62	-17.87

The fluid-film bearing model also accounts for pressure losses due to centrifugal flow effects through the feed orifices. Since the bearing ring does not rotate, the outer film centrifugal pressure loss factor is zero. An assumed 0.25 centrifugal pressure loss factor for the inner film is used.

Bearing material properties are important in determining clearance changes due to material thermal growth. During testing, shaft, housing, and ring temperatures were not measured. A reasonable estimation of the shaft temperature is made using an assumed turbine inlet temperature of 700°C and a defect temperature ratio. The defect temperature ratio as defined in Ref. [27] is

$$\theta_j = \frac{T_j - T_{oil\ inlet}}{T_{turbine\ inlet} - T_{oil\ inlet}} \tag{1}$$

where j indicates the measurement location. Recent shaft temperatures measured on a separate TC unit [27] suggests θ =0.16 is reasonable for shaft temperatures at the turbine bearing. Using an average oil inlet temperature, the shaft temperature is estimated to be ~205°C. Please note that in the bearing thermal model, the shaft surface is considered to be adiabatic (i.e. no heat transfer to or from the inner film).

Housing temperature estimates follow from direct measurements [1] of center housing temperatures obtained from a TC installed a passenger vehicle. The data suggest 150°C is a reasonable estimation. Ring temperatures are calculated by the model using an initial guess of 178°C.

Figure 7 depicts the predicted exit film temperatures for the inner film and outer film of the compressor bearing end at three engine loads. The lubricant supply temperature is shown to depict film temperature rise. Turbine bearing end predictions are nearly identical to compressor bearing end predictions; and not shown for brevity. Expectedly, the inner film temperature is greater than the outer film temperature since the inner film dissipates more power. Note that the temperature rise, defined as the difference between exit film temperature and supply temperature, decreases for the outer film with increasing shaft speed.

[1] Measurements conducted in personal vehicle

Figure 8 compares predicted power losses at the inner film of the compressor bearing end for three engine loads. Power losses are only significant for the inner film, as only the inner film is subjected to viscous shear caused by the rotating shaft. Since the ring does not rotate, the outer film acts solely as a squeeze-film damper (no viscous shear) and therefore consumes a negligible amount of mechanical energy.

Figure 9 illustrates predicted lubricant effective viscosities (lubricant viscosity at effective film temperature) for increasing shaft speeds. The lubricant viscosity decreases with increasing shaft speed due to increased film temperatures and an increase in drag power loss (i.e. higher shear forces). Note that the inner film viscosity decreases more rapidly than the outer film viscosity.

Thermal growth of the bearing (shaft, ring, and housing) due to increasing lubricant temperatures causes the bearing clearances to change, as shown in Figure 10. The figure shows bearing clearances with respect to nominal cold temperature radial clearances. As shaft speed increases, inner film clearance increases while outer film clearance decreases, indicating expansion of the ring.

Figure 11 demonstrates the inlet film pressure loss due to centrifugal flow effects for the inner film. Since the lubricant supply pressure changes, predicted inlet film pressures presented are relative to the lubricant supply pressure. Expectedly, the inlet film pressure decreases only for the inner film as only the TC shaft is rotating. Note that the inner film becomes starved of lubricant at ~100 krpm. Above this speed, the model assumes an inlet film pressure of 0.1 bar to prevent the calculations from collapsing. Such film starvation can lead to oil coking or even reversion of lubricant flow (inner film to outer film)!

Pertinent bearing parameters including lubricant viscosity, clearances, inlet film pressures, side loads, and ring speed ratios (non-zero for FRBs) are input into a linear rotordynamics model to predict RBS damped natural frequencies and mode shapes (eigenvalue analysis) as well as the linear response to imbalance. Section V presents the predicted results and comparisons to test data.

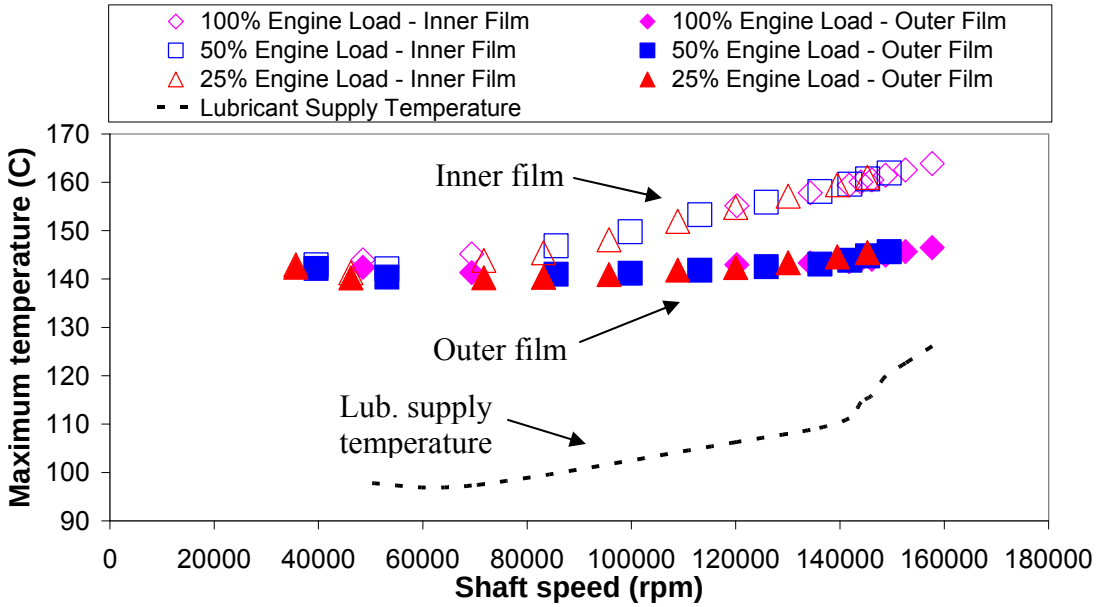

Figure 7. Predicted exit inner and outer film temperatures at compressor bearing for bearing parameters at 25%, 50%, and 100% engine loads

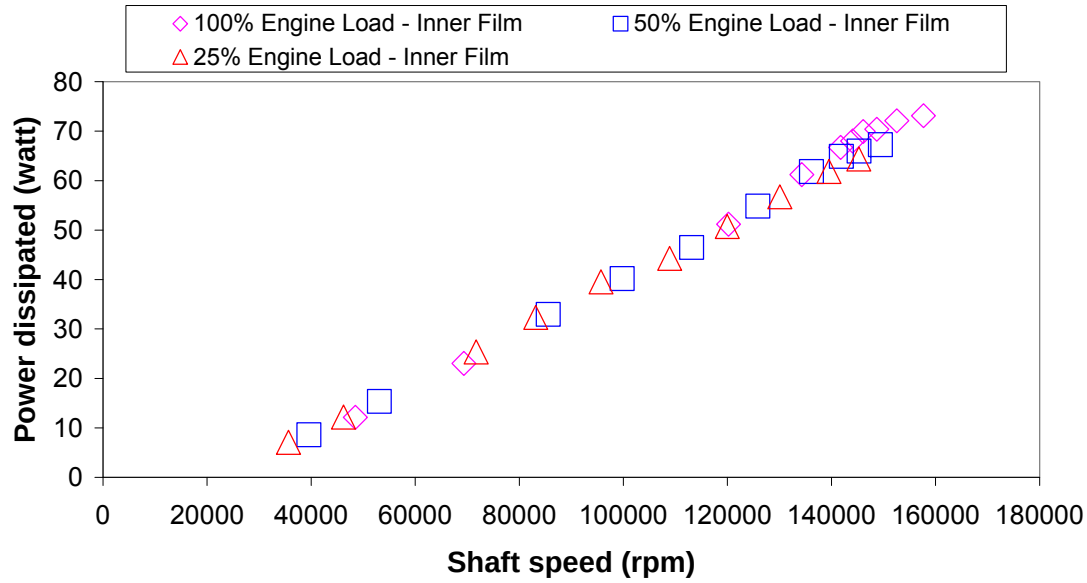

Figure 8. Predicted power losses at the inner film of the compressor bearing end for bearing parameters at 25%, 50%, and 100% engine loads

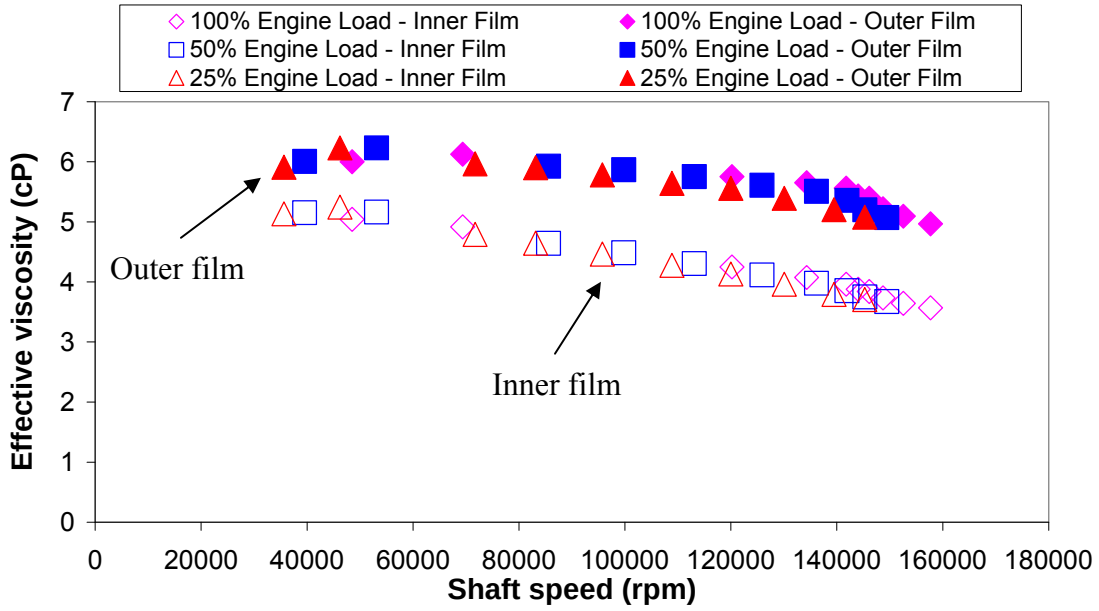

Figure 9. Predicted effective lubricant film viscosity of the compressor bearing end for bearing parameters at 25% 50%, and 100% engine loads

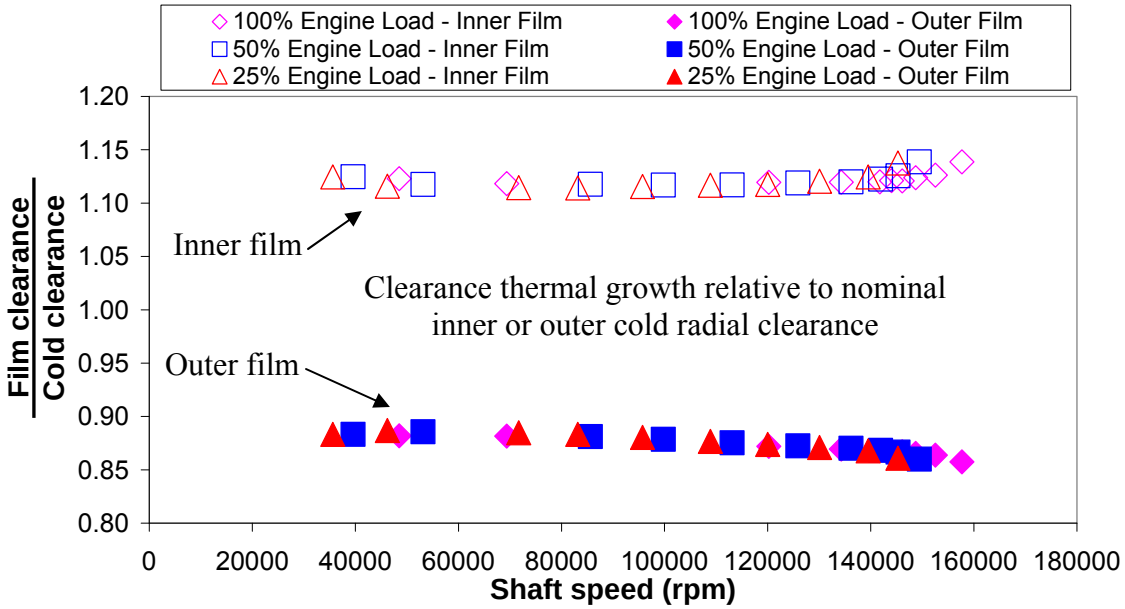

Figure 10. Predicted inner and outer film clearances relative to nominal cold radial clearances of the compressor bearing end for bearing parameters at 25%, 50%, and 100% engine loads

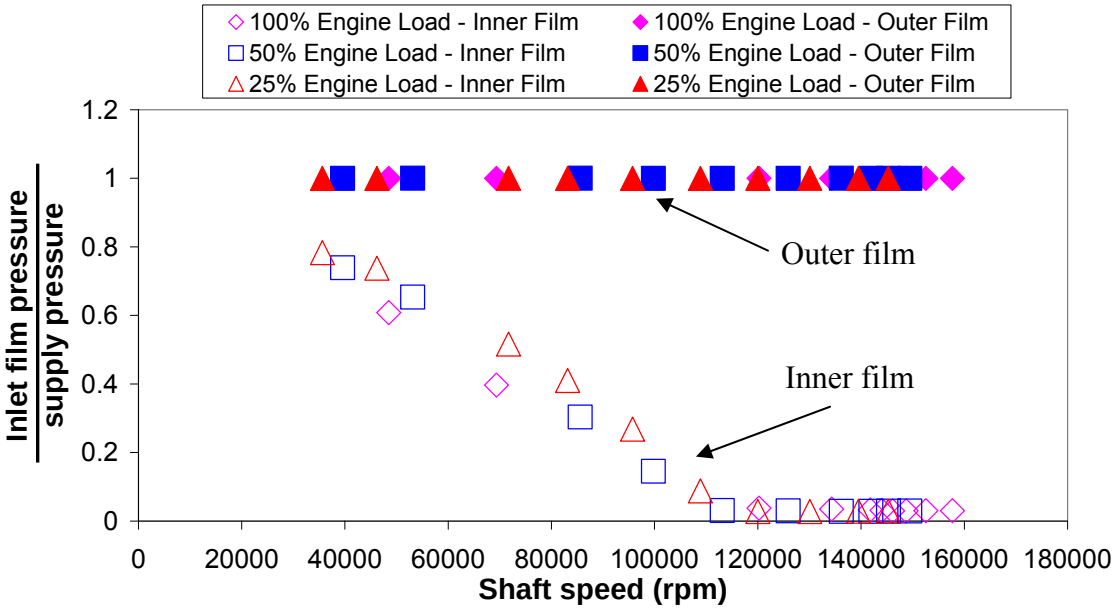

Figure 11. Predicted inlet film pressure to supply pressure ratio at the compressor bearing end for bearing parameters at 25%, 50%, and 100% engine loads

IV ANALYSIS OF HOUSING ACCELERATION TEST DATA AND METHODOLOGY OF INTEGRATING TEST DATA INTO ROTORDYNAMICS PROGRAM

Figure 12 shows a photograph of the test rig setup for measuring TC shaft motions on an engine test stand. Two displacement transducers, affixed to the compressor housing and facing the TC shaft, are positioned in the horizontal and vertical planes. A third displacement transducer can also be positioned in the axial plane of the rotor to measure rotor axial vibrations. In practice, shaft motion measurements are always taken at the compressor shaft nose. The time data collected are converted into the frequency domain via Fast Fourier Transformations (FFTs) for further analysis.

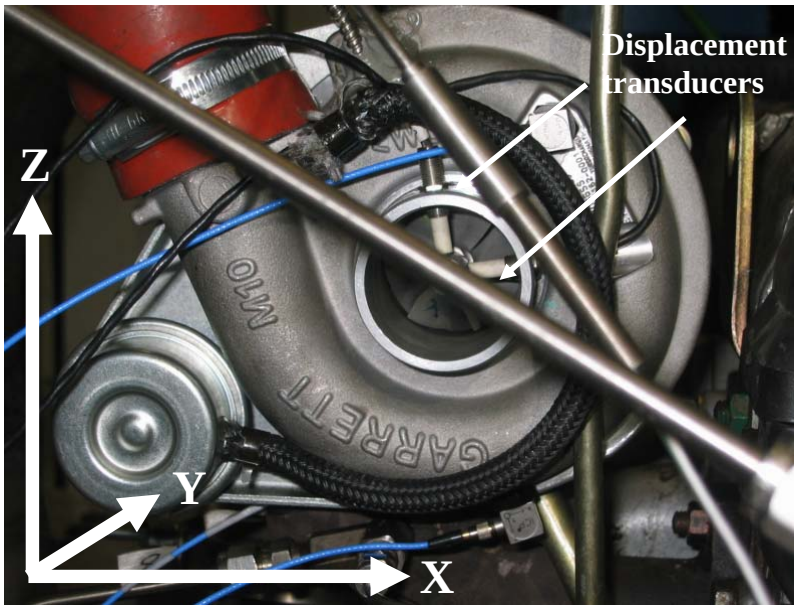

Figure 12. On-engine test rig setup for measuring TC shaft motions. Taken from Ref. [28]

Recently, the effects of engine-induced vibrations on TC rotor motion have become of interest. Thus, in addition to shaft motion measurements, the TC manufacturer has provided time data of TC center housing and compressor housing accelerations collected with a three-axes accelerometer. This section details an analysis of the TC housing acceleration test data.

Analysis of TC Housing Acceleration Test Data

Center housing and compressor housing vibrations are recorded on a TC mounted on a 4-cylinder engine test stand. The test data includes measurements in both horizontal and vertical directions at three engine loads: 25%, 50%, and 100 % of full engine load. Figure 13 shows the placement of the three-axes accelerometers.

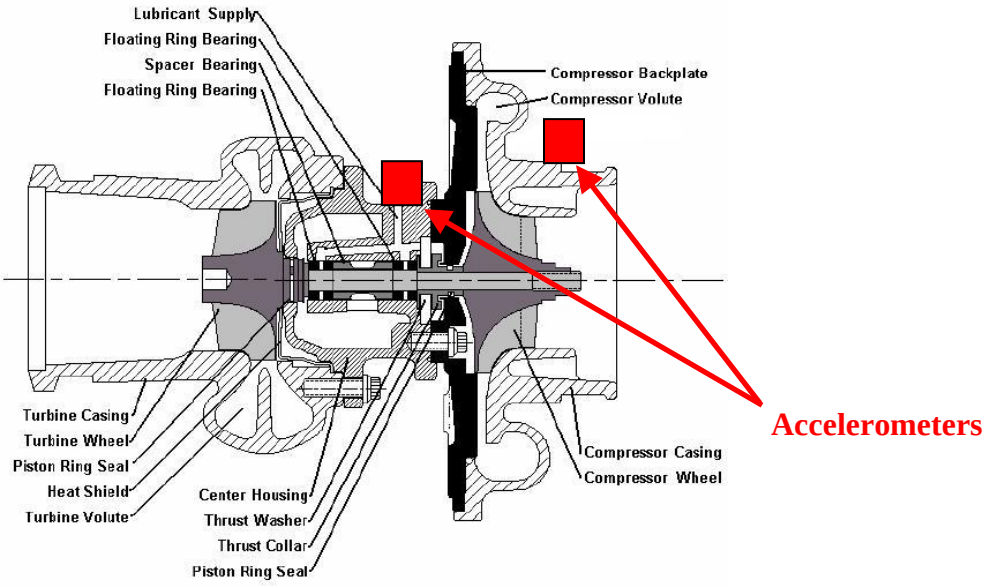

Figure 13. Typical TC schematic showing placement of accelerometers on center housing and compressor housing

Using computer software, test data waterfalls are constructed for analysis. Table 3 shows the parameters used to construct the waterfalls. Each time data file contains 15,000 data points, of which, the last 2,048 points are used for the FFT analysis.

Table 3. Test data analysis parameters

Δt [μs]	Max Time [s]	# of data points used for FFT --	Δf [Hz]	Max FFT freq. [Hz]
200	3.0	2,048	2.44	2,500

Since all three engine loads display similar vibration characteristics, only waterfalls for 100% engine load are presented. Appendix A includes waterfalls for the other engine loads. Ref. [29] details the analysis of the test data.

Table 4 lists the engine and TC speeds as well as TC oil feed conditions for 100% engine load. Please note that the *y*-axis scaling and/or maximum FFT frequency of the waterfalls presented do not show the TC synchronous response. The TC synchronous amplitude is either too small and/or occurs at too high a frequency.

Table 4. Engine and TC operating conditions at 100% of full engine load

100% Engine Load			
Engine Speed [rpm]	TC Speed [rpm]	TC Oil Supply Pressure [bar]	TC Oil Supply Temperature [°C]
1,000	48,504	1.3	97.9
1,250	69,366	1.7	97.3
1,750	120,216	2.2	106.3
2,000	134,298	2.4	108.8
2,250	141,762	2.5	111.2
2,500	144,036	2.6	114.6
2,750	146,106	2.8	116.0
3,000	148,722	2.7	119.9
3,250	152,532	2.7	122.6
3,600	157,674	2.7	126.1

Figure 14 shows waterfalls of center housing and compressor housing acceleration along the vertical direction for 100% engine load. Figure 15 displays the same waterfalls in terms of orders (or multiples) of main engine speed. At the outset of this research, the TC housing and its components were assumed to move as a rigid body, as all components are apparently rigidly connected. However, the results shown in Figure 14 clearly demonstrate this assumption is not correct; the center housing and compressor housing show very different vibration frequency contents. Typically, center housing vibration amplitudes are much smaller than compressor housing amplitudes, due to the high stiffness of the center housing.

Figure 16, comparing center housing and center housing total acceleration in the vertical direction, illustrates that compressor housing total acceleration is approximately twice that of center housing total acceleration. Ref. [29] shows recent finite element analysis (FEA) of the combined TC and exhaust manifold natural frequencies and mode shapes (see Figure 17) conducted by the TC manufacturer, which suggest that vibrations at ~300 Hz and ~570 Hz are due to system natural frequencies.

Figure 15 illustrates that *2e, 4e, 6e* order frequencies contribute significantly to the TC housing motion. This is most likely due to the engine firing frequency equaling two times the engine rotational speed. Interestingly, the engine synchronous frequency does not appear in the waterfall spectra.

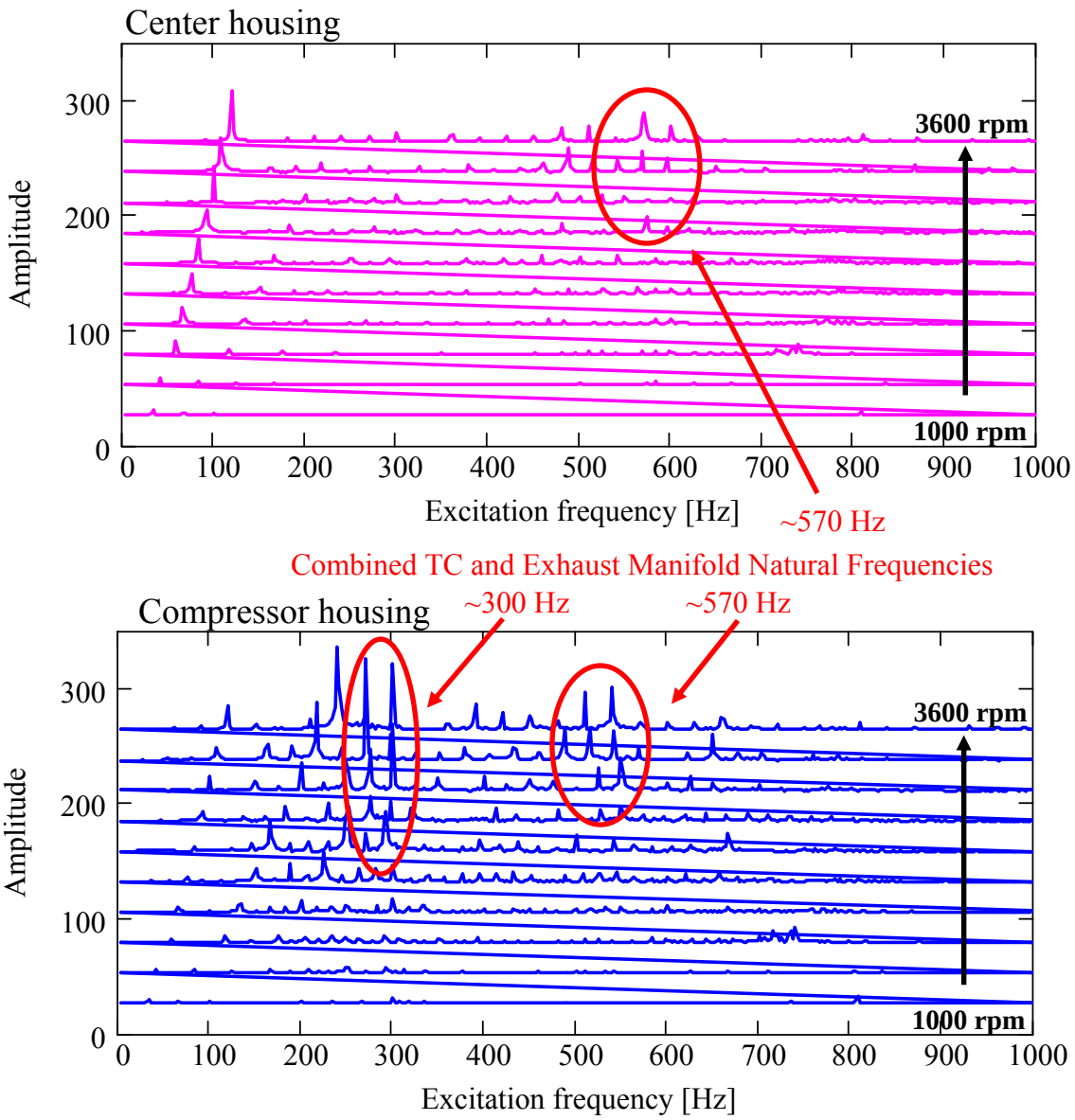

Figure 14. Waterfalls of center housing (top) and compressor housing (bottom) acceleration test data. 100% engine load, vertical direction

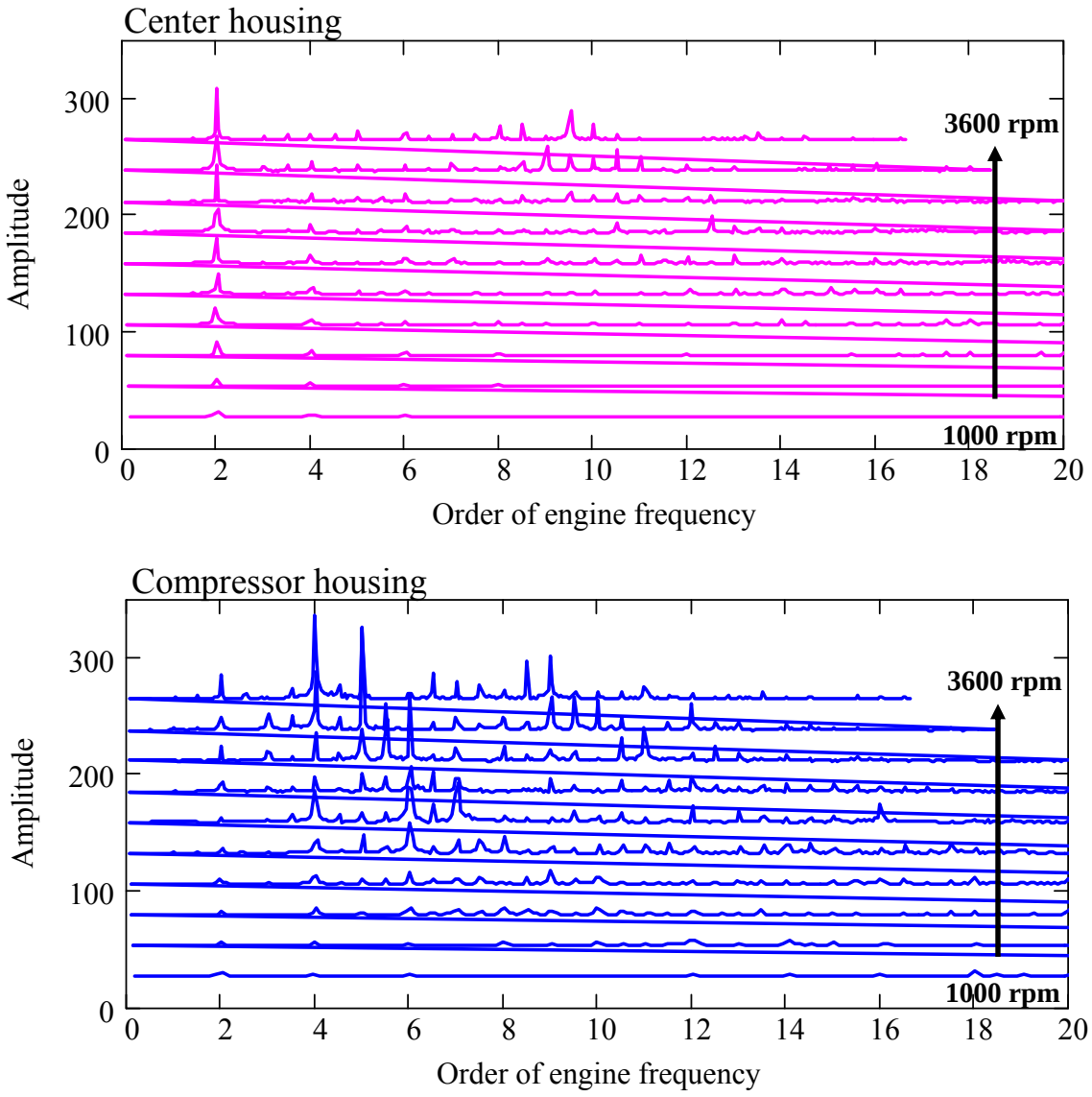

Figure 15. Waterfalls of center housing (top) and compressor housing (bottom) acceleration test data in terms of orders of engine frequency. 100% engine load, vertical direction

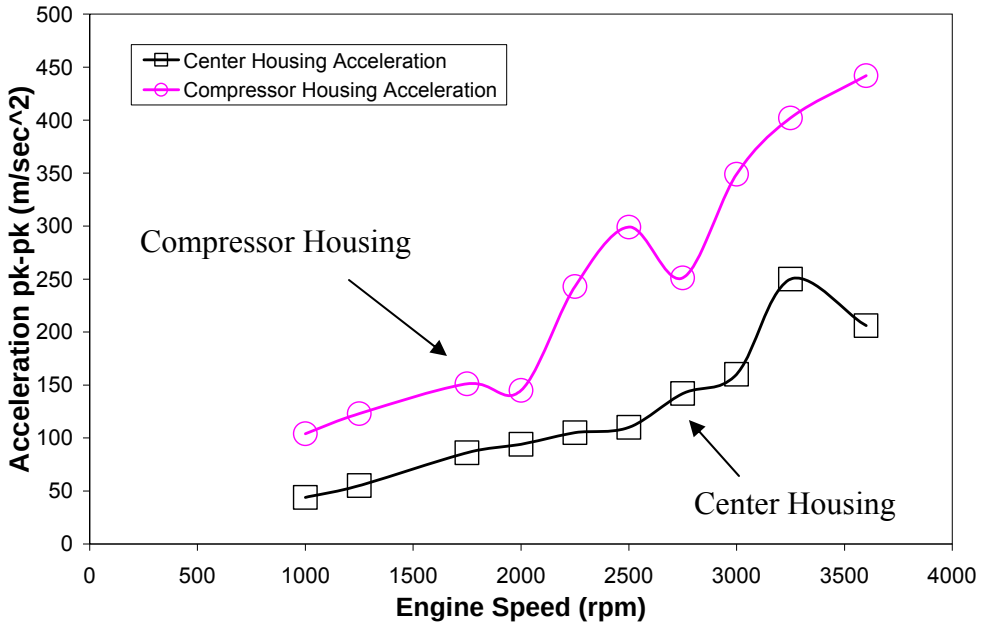

Figure 16. Center housing and compressor housing (pk-pk) acceleration along the vertical direction

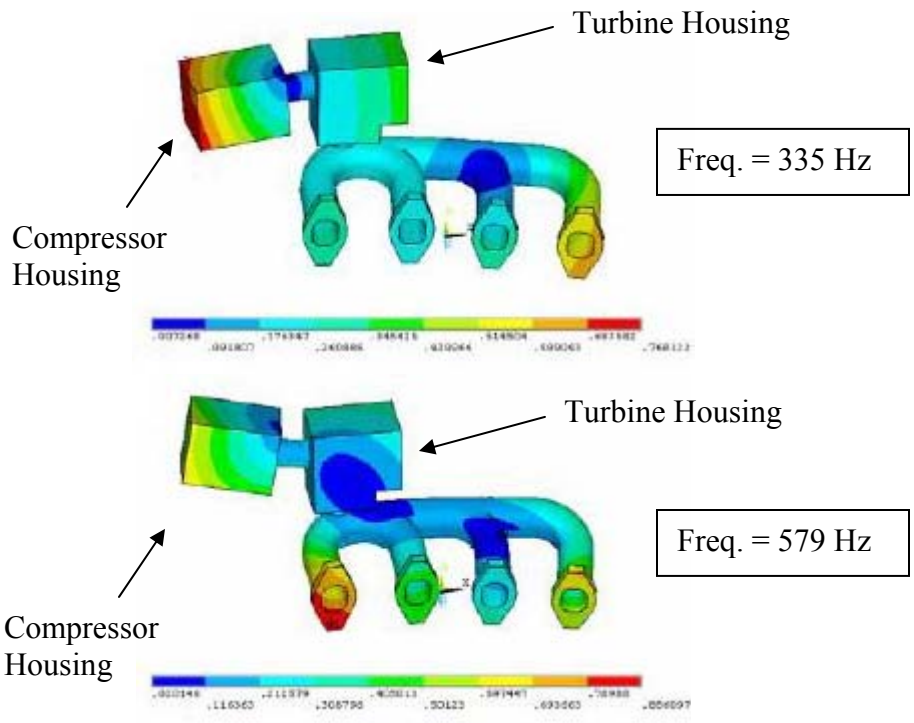

Figure 17. Combined manifold and TC mode shapes at 335 Hz (top) and 579 Hz (bottom). Taken from Ref. [30]

Integration of Test Data into Rotordynamics Program

Proper integration of the test data into the rotordynamic program requires accurate modeling of the housing acceleration. Using a computer program, a Fourier decomposition of the time data is performed. To simplify the calculations, the housing is assumed to move as a rigid body due to its heavy weight and thick-walled construction. Housing vibrations are assumed to be transmitted to the rotor only through the bearing connections. Also, the respective bearing connections are assumed to transmit identical housing vibrations, meaning that the housing is assumed to only move vertically or horizontally (no pitching or tilting). Given TC housing acceleration as a function of time, *a(t)*, with a fundamental engine frequency, ω_e, a Fourier coefficient decomposition of the time data gives,

$$a(t) = \cancelto{0}{A_0} + \sum_{n=1}^{N_F} A_n \cos\left(n\omega_e t + \phi_n\right) \tag{2}$$

where A_n and ϕ_n are the magnitude and phase of the *n*th order of the fundamental engine frequency (maximum frequency order = N_F).

Performing double time integration of Eq. 2 and assuming null initial conditions in displacement and velocity yields housing displacement, *x(t)*.

$$x(t) = \sum_{n=1}^{N_F} -\frac{A_n}{\left(n\omega_e\right)^2} \cos\left(n\omega_e t + \phi_n\right) \tag{3}$$

Currently, the rotordynamics program calculates only shaft displacement relative to an absolute coordinate system. It is important to realize that shaft motion test data is actually *motion relative to the compressor housing*. Thus, shaft motion relative to the TC housing must be calculated to properly quantify the effect of housing motion on TC shaft motion and to accurately reproduce test conditions. However, this task is relatively simple as absolute housing displacements are already known. Assuming the phase difference between the shaft and TC housing displacements is negligible[2], calculation of TC shaft motion relative to its housing follows as absolute shaft displacement minus

[2] In the tests, the measurements of shaft displacements and TC housing acceleration were not recorded simultaneously. Hence, then the assumption used.

housing displacement. The first ten Fourier coefficients (including half-orders) are used to model housing accelerations. For brevity, Appendix B lists all center housing and compressor housing Fourier coefficient and phase angle inputs into the rotordynamics program for 100% engine load only.

V LINEAR AND NONLINEAR TC RESPONSE PREDICTIONS WITH ENGINE-INDUCED HOUSING EXCITATIONS: COMPARISONS TO TEST DATA

This section presents the results of linear and nonlinear (time transient) analyses and compares predicted shaft motion to test data. Predictions are obtained for each engine load: 25%, 50%, and 100% of full engine load. However, the linear and nonlinear analyses for all engine loads show either nearly identical results or similar trends, respectively. Thus, for brevity, only results for 100% engine load are discussed. Predictions (and test data) in all figures shown below correspond to vertical motion (*y*-direction) at the compressor nose. In addition, all shaft motion amplitudes are presented relative to the maximum conical motion at the compressor nose (0.324 mm 0-pk). Nonlinear predictions presented are motion relative to the compressor housing with engine-induced excitations unless otherwise specified. Test data always includes engine-induced excitations and is always denoted as solid, red diamonds: ◆

Linear Analysis

The linear analysis consists of an eigenvalue analysis to determine system natural frequencies and corresponding rotor mode shapes as well as construction of an imbalance response plot. The analysis uses linearized bearing stiffness and damping force coefficients calculated from the SFRB model.

Figure 18 shows the predicted damped natural frequency map for 100% of full engine load. The map evidences four forward precessional rotor natural frequency mode shapes: a rigid conical mode, two cylindrical mode shapes, and the first elastic mode. However, only the first elastic mode shape corresponds with a rotor critical speed at ~150 krpm.

Figure 19 shows predicted rotor mode shapes, along with frequency and damping ratio, at 80 krpm. The lowest frequency mode shape is a well-damped rigid conical mode (f = 99 Hz, ξ = 0.32). The next mode shape is a rigid cylindrical mode characterized by

large compressor wheel and compressor bearing end motions (f = 546 Hz, ξ = 0.25). Closely following is another rigid cylindrical mode, characterized by large motions at the turbine bearing end. This mode shape is well-damped (f = 621 Hz, ξ = 0.53). The highest frequency mode shape is the lightly-damped first elastic mode (f = 2,025 Hz, ξ = 0.14).

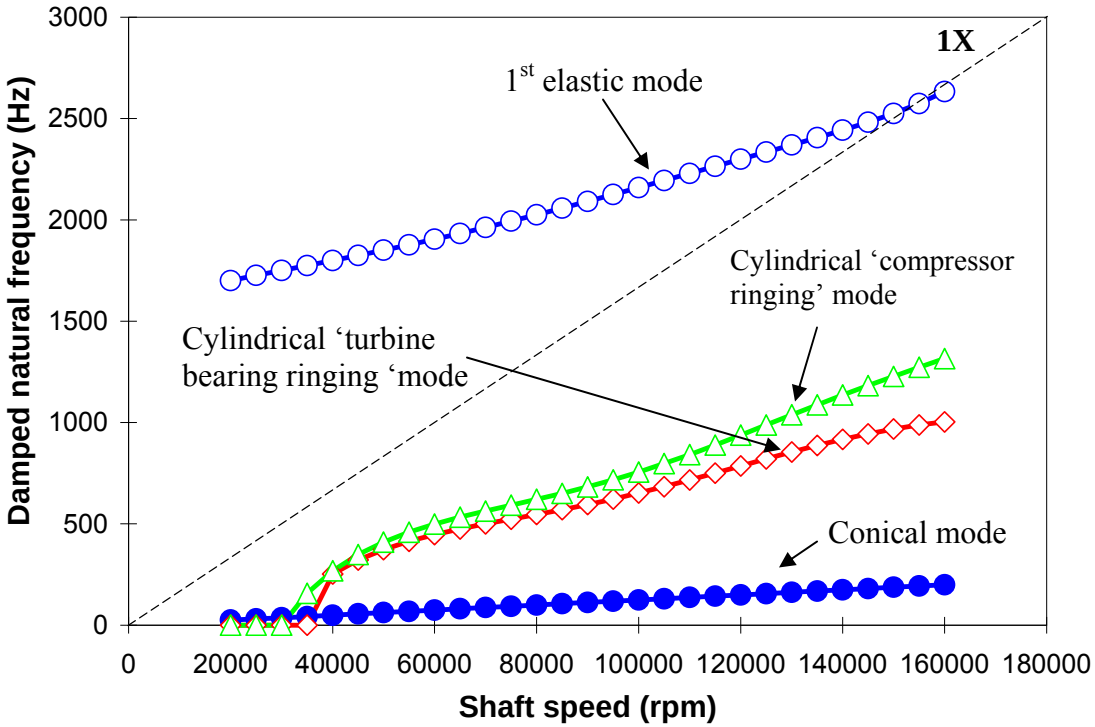

Figure 18. TC damped natural frequency map for 100% engine load

Figure 20 compares predicted linear imbalance response to test data. Shaft amplitudes presented in this section are relative to the maximum conical motion (0.324 mm 0-pk) at the compressor shaft end. Predictions from time transient simulations (nonlinear analysis) are also shown for comparison. A full description of the nonlinear analysis is presented later in this section. Note that two sets of nonlinear predictions are shown: with and without housing excitation. Both linear and nonlinear predictions under-predict test data, although linear predictions correlate with test data at high shaft speeds (>140 krpm). Both predictions and test data show increasing synchronous amplitudes with shaft speed. The disparity between predictions and test data is attributed to an inaccurate knowledge of the actual TC imbalance.

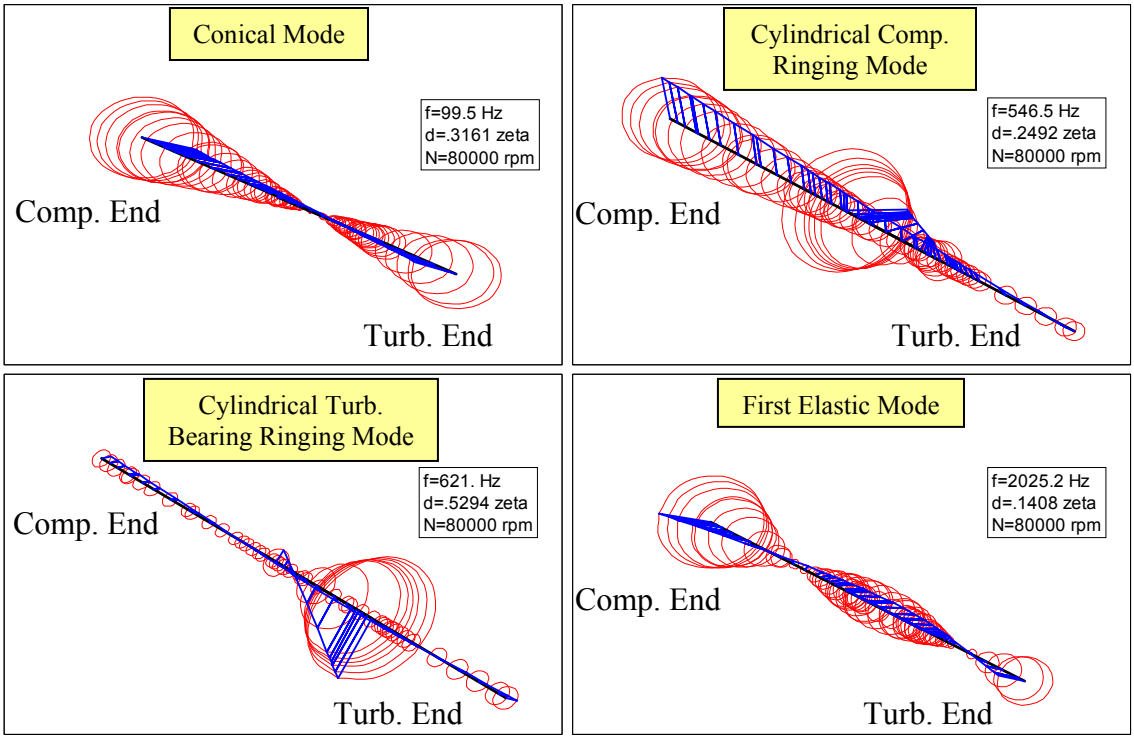

Figure 19. Predicted rotor natural frequency mode shapes at 80 krpm, 100% engine load. Rigid conical mode (top left), rigid cylindrical 'compressor ringing' mode (top right), rigid cylindrical 'turbine bearing ringing' mode (bottom left), first elastic mode (bottom right)

Also, both sets of nonlinear predictions show identical responses for all shaft speeds. The result is expected since housing accelerations occur at much lower frequencies than shaft synchronous frequencies.

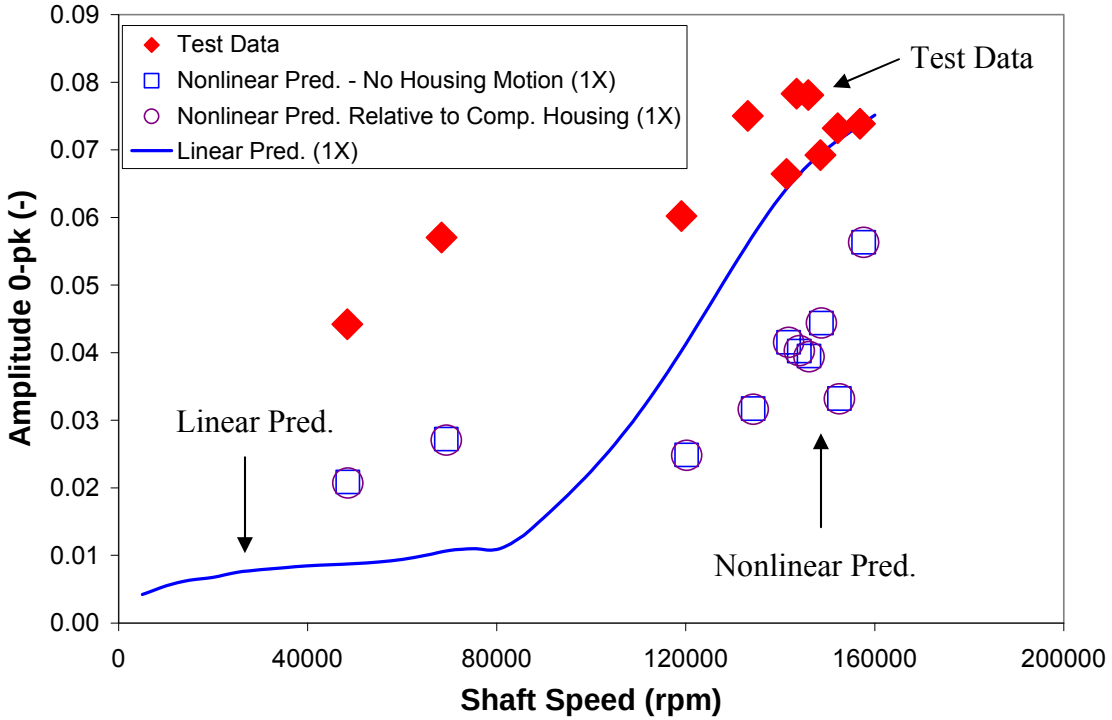

Figure 20. Comparison of predicted linear and nonlinear synchronous TC shaft response to test data (compressor nose, vertical direction)

Nonlinear Analysis

As shown previously in Refs. [12-16], linear analyses are unable to predict subsynchronous (nonlinear) responses. Thus, to accurately and completely predict RBS responses, nonlinear (time transient) computational schemes must be employed. The equations of motion are integrated in time, with bearing forces calculated at each time step. The nonlinear analysis is conducted at engine speeds ranging from 1,000 rpm (48.5 krpm TC shaft speed) to 3,600 rpm (157.5 krpm TC shaft speed).

Table 5 lists the nonlinear time transient parameters used for this analysis.

Table 5. Nonlinear time transient parameters

Time Step Size [μs]	Maximum Integration Time [s]	No. of Time Steps [-]	Minimum Frequency Step Size [Hz]	Maximum Frequency [Hz]
78.125	1	12,800	4	6,400

The time integration results are transformed to the frequency spectrum via Fast Fourier Transformations (FFTs). However, only the last 4,096 time data points are used,

resulting in a 3.12 Hz step size. Note that shaft amplitudes presented in this section are relative to the maximum conical motion (0.324 mm 0-pk) at the compressor shaft end.

Figure 21 displays waterfalls of shaft motion for predicted shaft motion with no engine-induced housing accelerations, predicted motion (relative to the compressor housing) with housing accelerations, and test data at the compressor shaft end. Predictions with no housing accelerations show very little subsynchronous response which is in direct contrast to predictions with housing accelerations and test data, which show a broad, low frequency response. Clearly, housing (i.e. engine) vibrations are the source of the low frequency response. It should be noted that test data uses a frequency step size of 10 Hz, resulting in a very rough spectrum.

Accurate prediction of TC total shaft motion is of the utmost importance in industry. Total shaft motion can be defined as either the maximum shaft orbit diameter (x vs. y plot) or maximum peak to peak amplitude (x vs. time or y vs. time) at the compressor nose. Predicted total shaft motion is determined using an orbit plot while test data is restricted to a single measurement plane. Typically, shaft orbit patterns are nearly circular (i.e. $x \approx y$) so calculating total motion using either method gives similar results. However, disparity can arise when orbit shapes are highly skewed.

Figure 22 compares the predicted total shaft motion to test data. At first glance, it appears that total motions are greatly over predicted at engine speeds < 2,500 rpm. However, as shown in the inset in Figure 22, TC housing engine-induced excitations cause a highly lop-sided orbit at low engine speeds, producing misleading comparisons. Note that the orbit size becomes more circular as engine speed increases. Manual calculations of predicted total shaft motion while restricting the calculations to the vertical plane only shows that total shaft motion is much better predicted than originally depicted (see Figure 23).

Figure 24 compares predicted and measured subsynchronous amplitudes at each engine speed. Peak amplitude values are also denoted in the plot and indicate whether the synchronous or subsynchronous vibration is the dominant amplitude at that particular engine speed. At the majority of engine speeds, engine-induced TC shaft vibrations

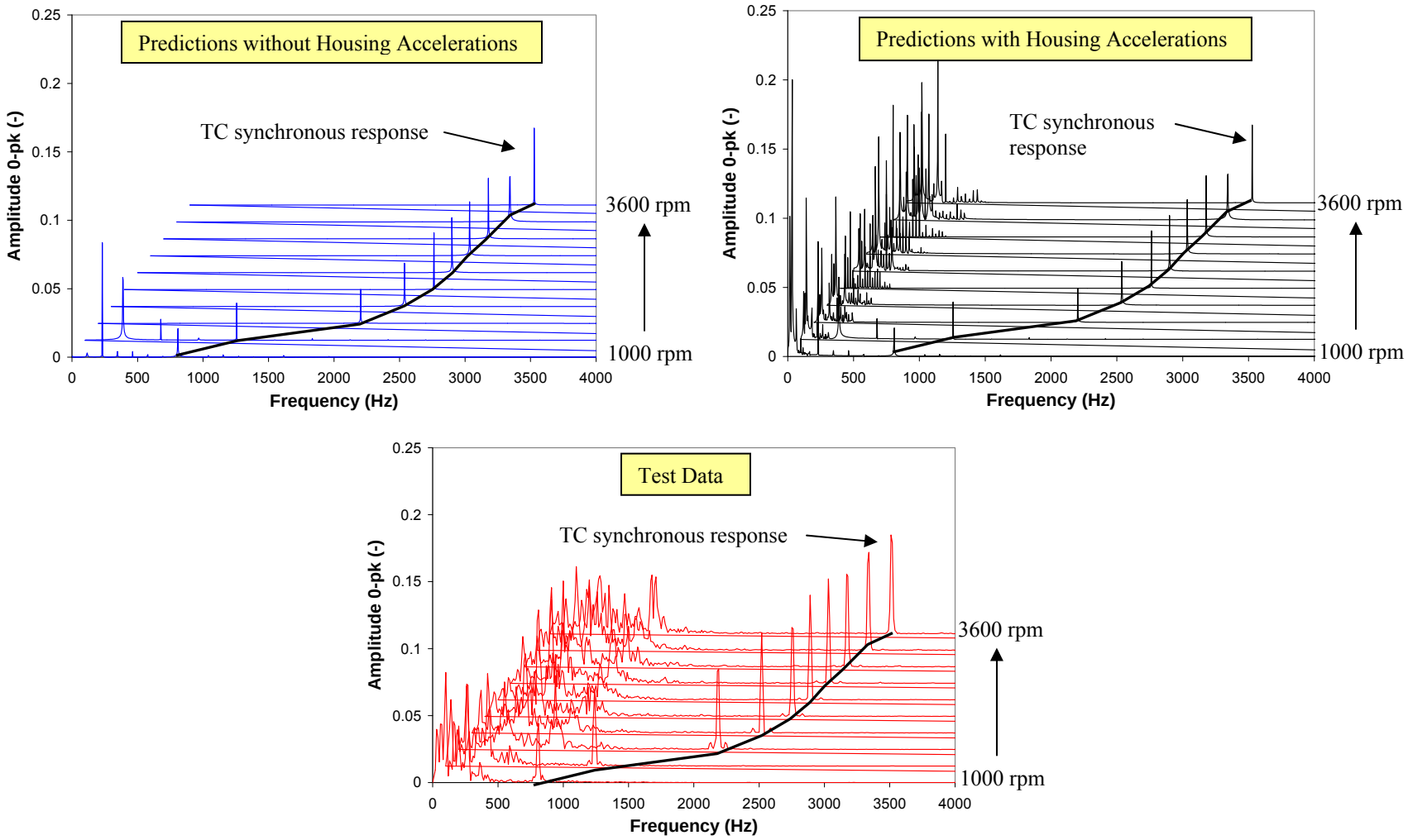

Figure 21. Waterfalls of shaft motion (compressor nose, vertical direction). Predictions with no housing accelerations (top left), predictions with housing accelerations (top right), test data (bottom)

contribute significantly to total shaft motion. Predictions agree remarkably well with test data, especially between 1,750 rpm – 3,000 rpm.

Figure 25 presents predicted and measured subsynchronous amplitudes in terms of orders of engine speed. Recall that only 10e order frequencies (including half-orders) are used to model housing vibrations and that *2e* and *4e* order frequencies are typically the dominant frequencies. As expected, *2e* and *4e* order frequencies induce marked shaft motion amplitudes, although predictions evidence vibrations up to only *7e* order frequencies. Test data, however, only shows minimal vibration amplitudes below 6e order frequency. It is unclear why higher engine order frequencies are not predicted.

Note that predicted amplitudes at *~14e* order frequency are *not* due to engine-induced housing excitations. Rather, the amplitudes are attributed to TC shaft self-excited subsynchronous vibrations, independent of its housing motion.

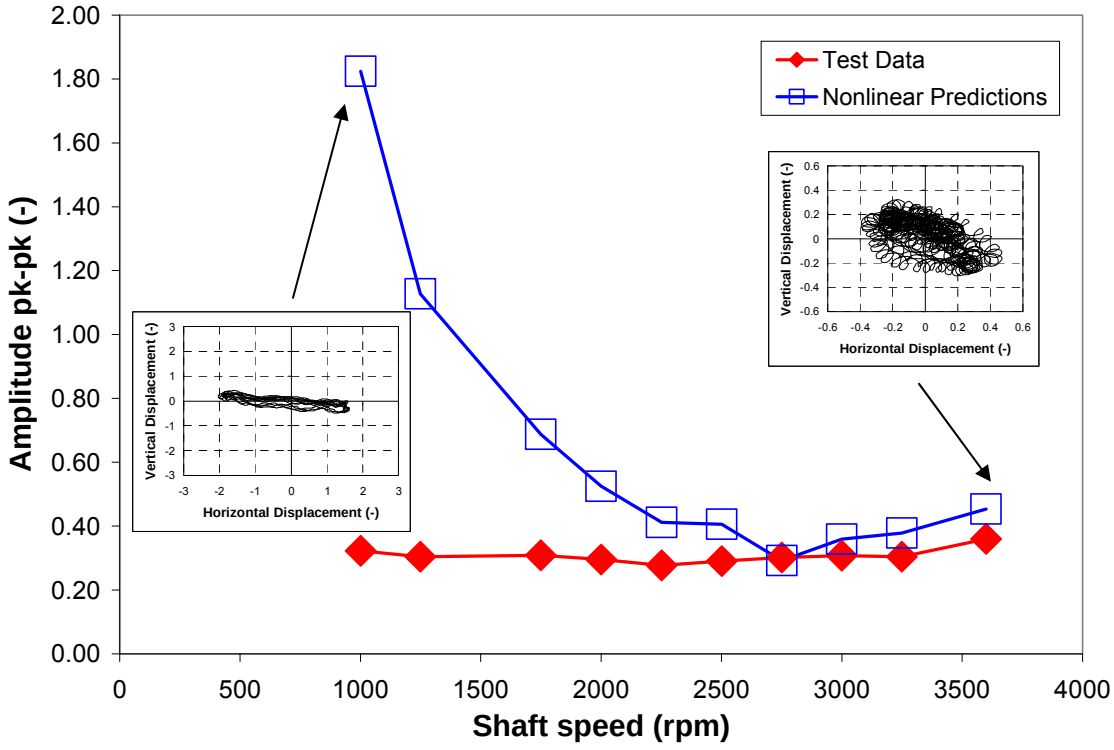

Figure 22. Total shaft motion, predicted and measured, vs. shaft speed. Predicted total motion derived from orbit plots. Insets show TC shaft orbit plot at indicated engine speed

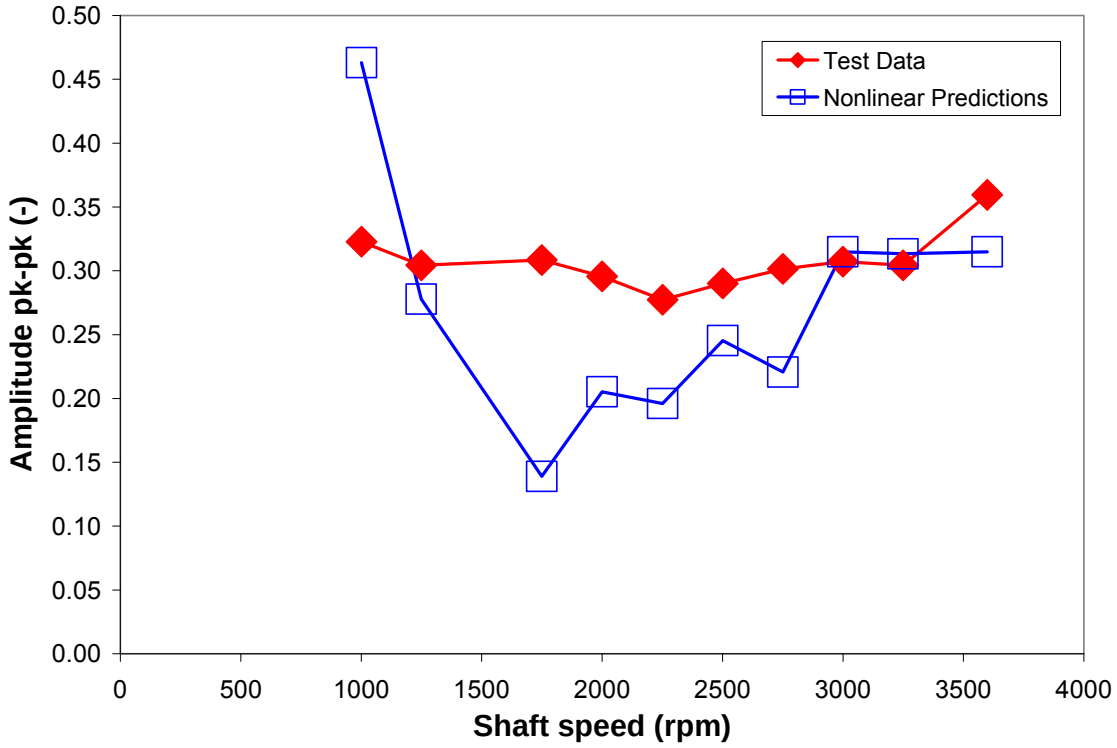

Figure 23. Total shaft motions, predicted and measured, vs. shaft speed. Predicted total motion derived from shaft motions along vertical direction only

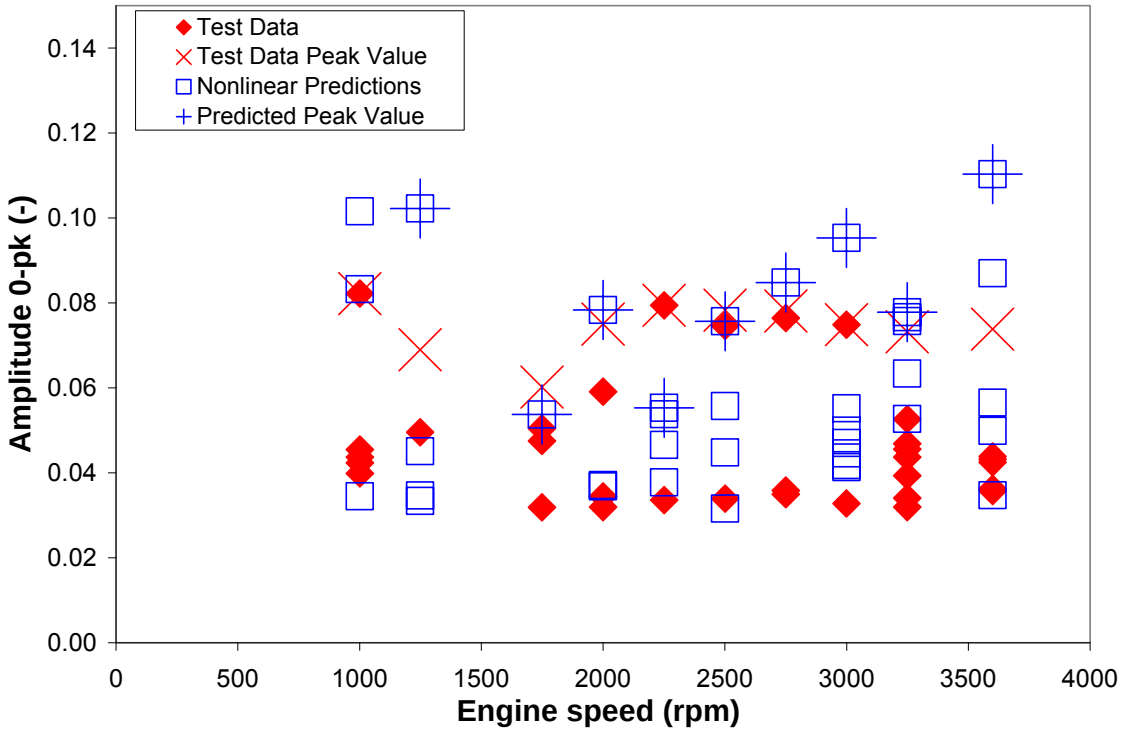

Figure 24. Predicted and measured subsynchronous amplitudes (compressor nose, vertical direction) vs. engine speed

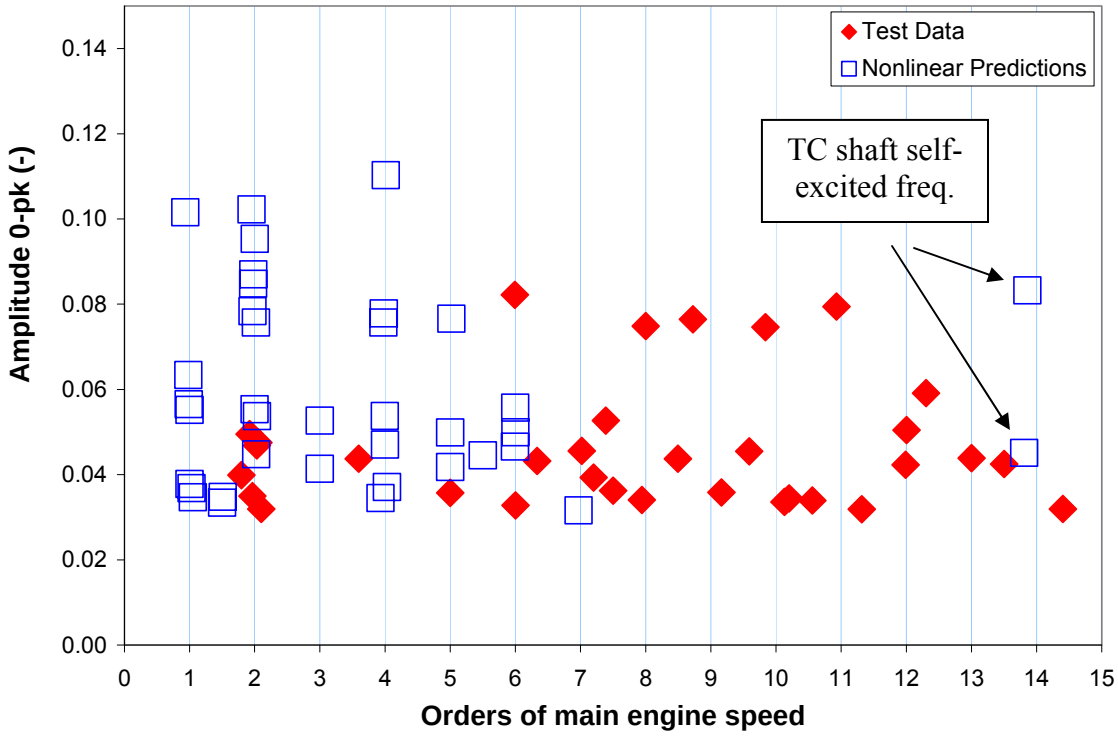

Figure 25. Predicted and measured subsynchronous amplitudes (compressor nose, vertical direction) vs. orders of engine speed

It should be noted that it is impossible to replicate the test data as housing accelerations (center housing and compressor housing) were not collected simultaneously with shaft vibration measurements. Also, the frequency step size used (10 Hz) is too large and fails to capture the shaft vibration amplitudes at frequencies coinciding with exact orders of engine speed.

Figure 26 shows comparisons of predicted and measured nonsynchronous frequencies versus TC shaft speed. The two solid black lines trace the *2e* and *4e* engine order frequencies, i.e. two and four times multiples of the fundamental engine frequency. Recall that *2e* and *4e* order frequencies contribute significantly to engine motion. As is the case in Figure 25, predictions only evidence low frequency vibrations and fail to predict frequencies higher than 300 Hz. Rotor damped natural frequencies are also plotted to determine if these frequencies are excited by any nonsynchronous vibrations. Although the *4e* order frequency tracks the rotor conical mode, no nonsynchronous vibrations are evidenced since the mode is well-damped. Still, the results demonstrate that engine super-harmonics can excite rotor natural frequencies. However, there are

several groupings of nonsynchronous frequencies that appear to track harmonics of the rotor conical mode: *Group 1* at one-half rotor conical mode (~ 30 – 120 Hz), *Group 2* at 2x rotor conical mode (~ 200 Hz – 500 Hz), and *Group 3* at 4x rotor conical mode (~ 650 Hz – 800 Hz). But these results are purely coincidental. *Group 1* is attributed to *2e* engine order frequency vibrations. *Group 2* is actually a mix of higher engine order frequency vibrations, as illustrated in Figure 27. And *Group 3* is clearly a super-harmonic of the second grouping.

Figure 27 also shows several nonsynchronous frequencies at 1,000 rpm (engine speed). Measurements by the TC manufacturer [29] indicate an engine operating natural frequency at 18 Hz, very close to 1,000 rpm (16.6 Hz).

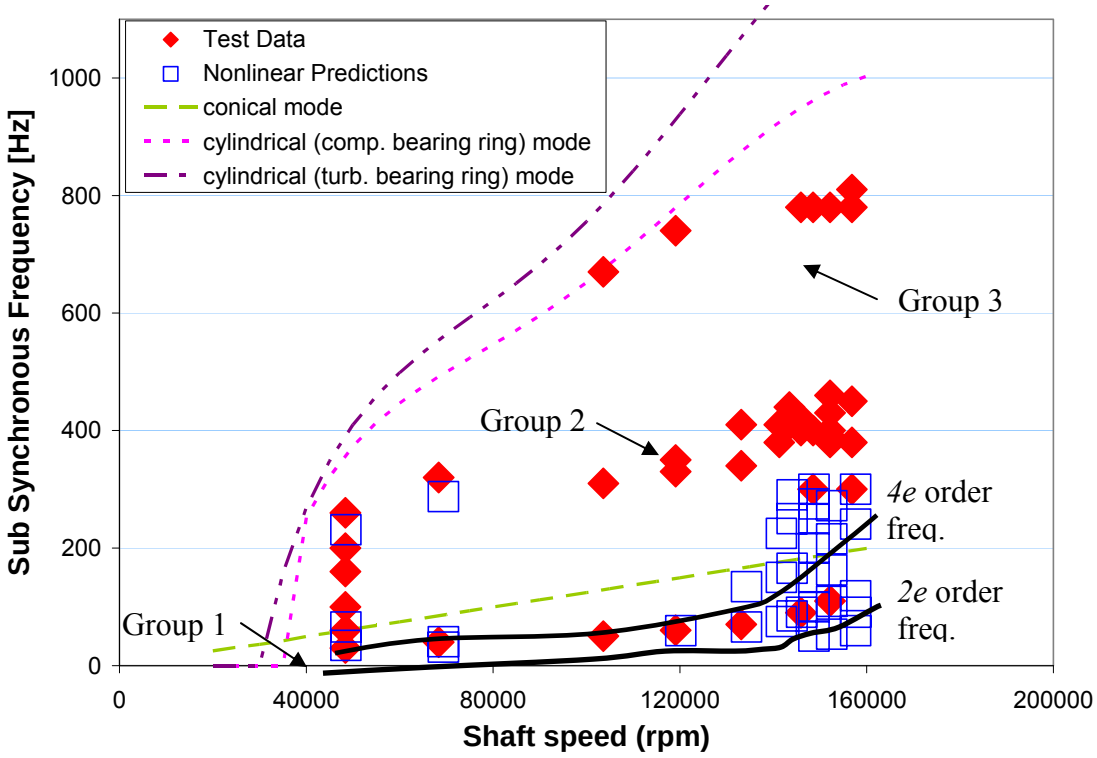

Figure 26. Predicted and measured shaft subsynchronous frequencies (compressor nose, vertical direction) vs. TC shaft speed

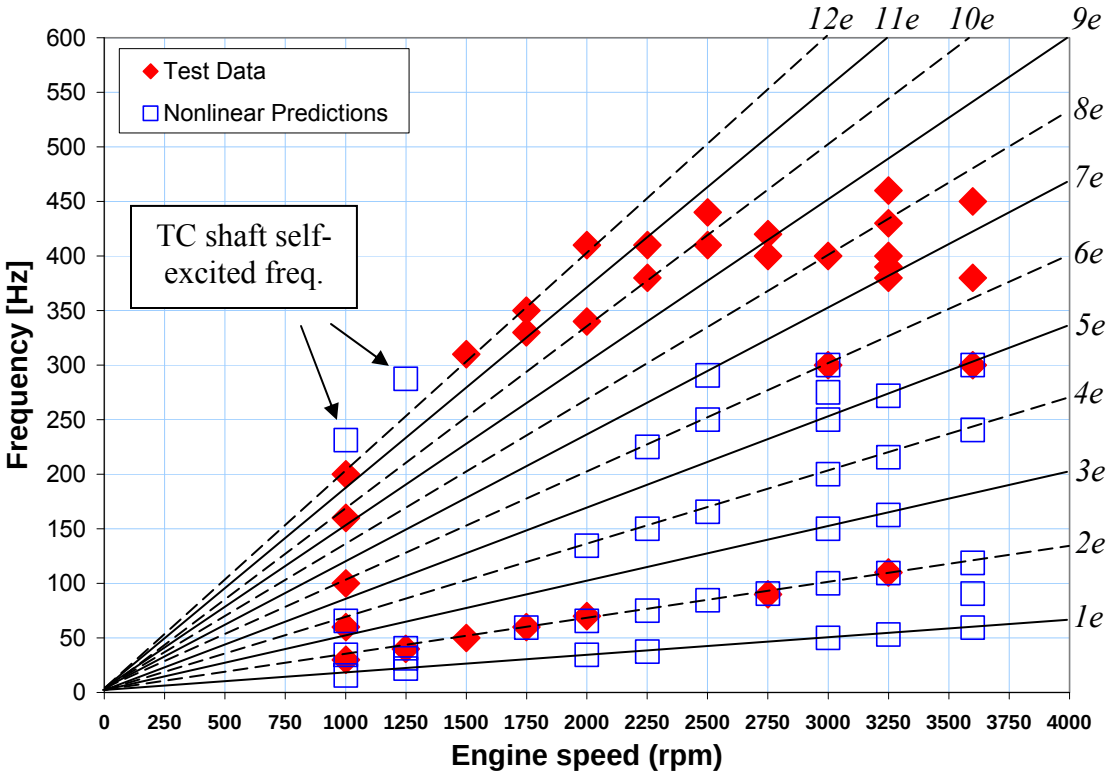

Figure 27. Predicted and measured shaft subsynchronous frequencies (compressor nose, vertical direction) vs. engine speed

VI CONCLUSIONS

This thesis presents progress on the refinement of linear and nonlinear rotordynamics models to accurately predict turbocharger (TC) shaft nonlinear forced response with engine-induced housing excitations. The results, measurements and predictions, demonstrate that engine vibrations cause a complex, low frequency TC shaft response, with significant frequencies at several multiple integers of engine speed. The most significant conclusions from this research are presented below.

Analysis of measured engine-induced housing accelerations shows that the center housing and compressor housing do not vibrate as a rigid body. The compressor housing deflects nearly twice as much as the center housing. However, both housings show marked amplitude responses at 2 and 4 order engine frequencies, most likely due to the engine firing frequency. Other order frequencies, including *5e* and *6e*, also contribute significantly to housing motion.

Linear eigenvalue predictions evidence four damped natural frequency TC shaft mode shapes, of which only the first elastic mode is lightly-damped (critical speed = 150 krpm). The TC top speed in tests was 160 krpm. Linear synchronous response predictions show that the amplitude increases with shaft speed, agreeing with test data only at the highest TC speeds. Nonlinear synchronous response predictions also show a similar trend, but still under-predict test data throughout the TC operating speed range. The differences between predictions and test data are attributed to an inaccurate knowledge of the actual TC imbalance distribution.

Nonlinear predictions of shaft motions with no housing accelerations show the TC is stable (i.e. no subsynchronous whirl) at all but the lowest operating speeds (<70 krpm). However, predictions of shaft motions with housing accelerations, as well as shaft motion test data, reveal shaft motions rich in subsynchronous activity throughout the entire speed range. The differences noted demonstrate the dramatic effect of engine-induced housing accelerations on TC shaft motions. The housing excitations also cause highly skewed TC shaft orbits at low engine speeds. These non-circular shaft orbits must be accounted for when determining TC total shaft motion. Predicted total shaft motions agree remarkably well with test data, differing by at most 0.11 mm pk-pk. Also, total shaft motion

amplitudes (relative to compressor housing) remain nearly constant with increasing engine speed, even though housing acceleration amplitudes increase with engine speed. This indicates the TC shaft is isolated from housing (and engine) motion. Agreement with test data is particularly good above engine speeds greater than 3,000 rpm (shaft speed ~ 148 krpm). Predicted TC subsynchronous amplitudes as well as peak vibration amplitudes also correlate well with test data, especially between 1,750 – 3,000 rpm. However, predictions indicate TC shaft vibrations are attributed to engine order frequencies *6e* and below, whereas measurements show marked amplitude responses at order frequencies greater than *6e*. The analysis also reveals that super-harmonics of the engine speed can excite TC damped natural frequencies, although in this instance the mode shape (rotor conical mode) is well-damped. Nonetheless, the results demonstrate the importance in including housing accelerations in TC system models.

Most importantly, the comparisons of predictions to test data serve to validate this first step in incorporating engine-induced housing excitations into the rotordynamics model. This research furthers the goal to create a virtual laboratory to aid a TC manufacturer in reducing development time and expenditures.

There are several opportunities for improvement. More comparisons between predictions and measurements should be made for other TCs and for different bearing configurations. Housing acceleration measurements should also be collected simultaneously with shaft displacement measurements and for smaller frequency steps sizes (larger time spans) to ensure accurate prediction of test data is possible. Further analysis of housing acceleration measurements is also needed to determine the cause of higher engine order frequencies and why these frequencies are not predicted. These steps will serve to definitively validate the rotordynamics model and provide a useful tool to industry.

REFERENCES

[1] Kerth, J., 2003, "Prediction and Measurement of the Rotordynamic Response of an Automotive Turbocharger with Floating Ring Bearings," M.S. thesis, Texas A&M University, College Station, TX.

[2] Sahay, S., and LaRue, G., 1997, "Turbocharger Rotordynamic Instability and Control," NASA CP3344, *Proceedings of the 1996 Conference on Rotordynamic Instability Problems in High-Performance Turbomachinery*, Cleveland, OH, pp. 247-257.

[3] Shaw, M. and Nussdorfer, T., 1949, "An Analysis of the Full-Floating Journal Bearing," Report No. 866, Nat. Advisory Committee Aeronautics, pp. 1-13.

[4] Tatara, A., 1970, "An Experimental Study of the Stabilizing Effect of Floating-Bush Journal Bearings," Bull. JSME, **13**(61), pp. 858-863.

[5] Rohde, S. M., and Ezzat, H. A, 1980, "Analysis of Dynamically Loaded Floating-Ring Bearings for Automotive Applications," J. Lubric. Tech.-T. ASME, **102**(3), pp. 271-277.

[6] Li, C. and Rohde, S., 1981, "On the Steady State and Dynamic Performance Characteristics of Floating Ring Bearings," J. Lubric. Tech.-T. ASME, **103**(3), pp. 389-397.

[7] Li, C., 1982, "Dynamics of Rotor Bearing Systems Supported by Floating Ring Bearings," J. Lubric. Tech.-T. ASME, **104**(4), pp. 469-477.

[8] Trippett, R., and Li, D., 1984, "High-Speed Floating-Ring Bearing Test and Analysis," ASLE Trans., **27**(1), pp. 73-81.

[9] Tanaka, M. and Hori, Y., 1972, "Stability Characteristics of Floating Bush Bearings," J. Lubric. Tech.-T. ASME, **94**(3), pp. 248-259.

[10] Holmes, R., Brennan, M., and Gottrand, B., 2004, "Vibration of an Automotive Turbocharger – A Case Study," Paper No. C623/011/2004, *IMechE Event Publications*, Professional Engineering Publishing, Suffolk, UK, **2004**(2), pp. 445-455.

[11] Holt, C., San Andrés, L., Sahay, S., Tang, P., LaRue, G., and Gjika, K., 2003, "Test Response of a Turbocharger Supported on Floating Ring Bearings – Part I: Assessment of Subsynchronous Motions," Paper No. DETC 2003/VIB-48418, *Proceedings of the ASME Des. Eng. Tech. Conf.*, ASME, New York, **5**(B), pp. 969-974.

[12] Holt, C., San Andrés, L., Sahay, S., Tang, P., LaRue, G., and Gjika, K., 2003, "Test Response of a Turbocharger Supported on Floating Ring Bearings – Part II: Comparisons to Nonlinear Rotordynamic Predictions," Paper No. DETC 2003/VIB-48419, *Proceedings of the ASME Des. Eng. Tech. Conf.*, ASME, New York, **5**(B), pp. 975-980.

[13] San Andrés, L. and Kerth, J., 2004, "Thermal Effects on the Performance of Floating Ring Bearings for Turbochargers," Proc. of the Inst. of Mech. Eng. Part J J. Eng. Tribol., **218**(5), pp. 437-450.

[14] San Andrés, L., Rivadeneira, J., Chinta, M., Gjika, K., and LaRue, G., 2007, "Nonlinear Rotordynamics of Automotive Turbochargers: Predictions and Comparisons to Test Data," J. Eng. Gas Turb. Power, **129**(2), pp. 488-493.

[15] Rivadeneira, J., 2005, "Predictions Versus Measurements of Turbocharger Nonlinear Dynamic Response," M.S. thesis, Texas A&M University, College Station, TX.

[16] San Andrés, L., Rivadeneira, J., Gjika, K., Groves, C., and LaRue, G., 2006, "A Virtual Tool for Prediction of Turbocharger Nonlinear Dynamic Response: Validation Against Test Data," Paper No. GT2006-90873, *Proc. of the ASME Turbo Expo*, ASME, New York, **5**(B), pp. 1313-1321.

[17] Gjika, K., and Groves, C., 2006, "Nonlinear Dynamic Behavior of Rotor-Bearing Systems Involving Two Hydrodynamic Oil Films in Series: Prediction and Test Application to High-Speed Turbochargers," Paper No. ESDA2006-95792, *Proceedings of 8th Biennial ASME Conf. on Eng. Syst. Design and Anal.*, ASME, New York, **2006**.

[18] Kirk, R., Alsaeed, A., Liptrap, J., Lindsey, C., Sutherland, D., Dillon, B., Saunders, E., Chappell, M., Nawshin, S., Christian, E., Ellis, A., Mondschein, B., Oliver, J., and Sterling J., 2006, "Experimental Test Results for Vibration of a High Speed Diesel Engine Turbocharger," *5th EDT & LMS Poitiers Workshop: "Bearing Behavior Under Unusual Operating Conditions,"* Poitiers, France.

[19] Hori, Y., and Kato, T., 1990, "Earthquake-Induced Instability of a Rotor Supported by Oil Film Bearings," J. Vib. Acoust. Stress, **112** (2), pp. 160-165.

[20] Lee, A., Kim, B., and Kim, Y., 2006, "A Finite Element Transient Response Analysis Method of a Rotor-Bearing System to Base Shock Excitations Using the State-Space Newmark Scheme and Comparisons With Experiments," J. Sound Vib., **297** (3-5), pp. 595-615.

[21] San Andrés, L., 2006, "Project Progress Report #34", Monthly Technical Report to Honeywell Turbo Technologies, August, Texas A&M University, College Station, TX.

[22] XLTRC^2™ Rotordynamics Software Suite v.2.20, 2004, Turbomachinery Laboratory, Texas A&M University, College Station, TX.

[23] San Andrés, L., 2006, XLFEMSFRB™ v6.0 Software Suite, Tribology Group, Turbomachinery Laboratory, Texas A&M University, College Station, TX.

[24] XLHydPad™ Software Suite, 1996, Turbomachinery Laboratory, Texas A&M University, College Station, TX.

[25] Xia., S, Test data received from Honeywell Turbo Technologies Shanghai, April 2, 2007.

[26] San Andrés, L., 2007, "Project Progress Report #42", Monthly Technical Report to Honeywell Turbo Technologies, June, Texas A&M University, College Station, TX.

[27] San Andrés, L., 2007, "Project Progress Report #41", Monthly Technical Report to Honeywell Turbo Technologies, May, Texas A&M University, College Station, TX.

[28] San Andrés, L., 2007, "Project Progress Report #40", Monthly Technical Report to Honeywell Turbo Technologies, April, Texas A&M University, College Station, TX.

[29] San Andrés, L., 2007, "Project Progress Report #43", Monthly Technical Report to Honeywell Turbo Technologies, July, Texas A&M University, College Station, TX.

[30] Guang, M., and JianPing, J., 2007, "Methodology for Translating Engine Vibration into Turbocharger for Rotordynamics Analysis", Report No. 15, May, Shanghai JiaoTong University, Shanghai, China.

APPENDIX A PREDICTED WATERFALLS OF SHAFT MOTION FOR VARIOUS ENGINE LOAD CONDITIONS

Figure A.1 and Figure A.2 show predicted waterfalls of shaft of motion relative to the compressor housing. Shaft amplitudes are presented relative to the maximum conical motion (0.324 mm 0-pk) at the compressor shaft end.

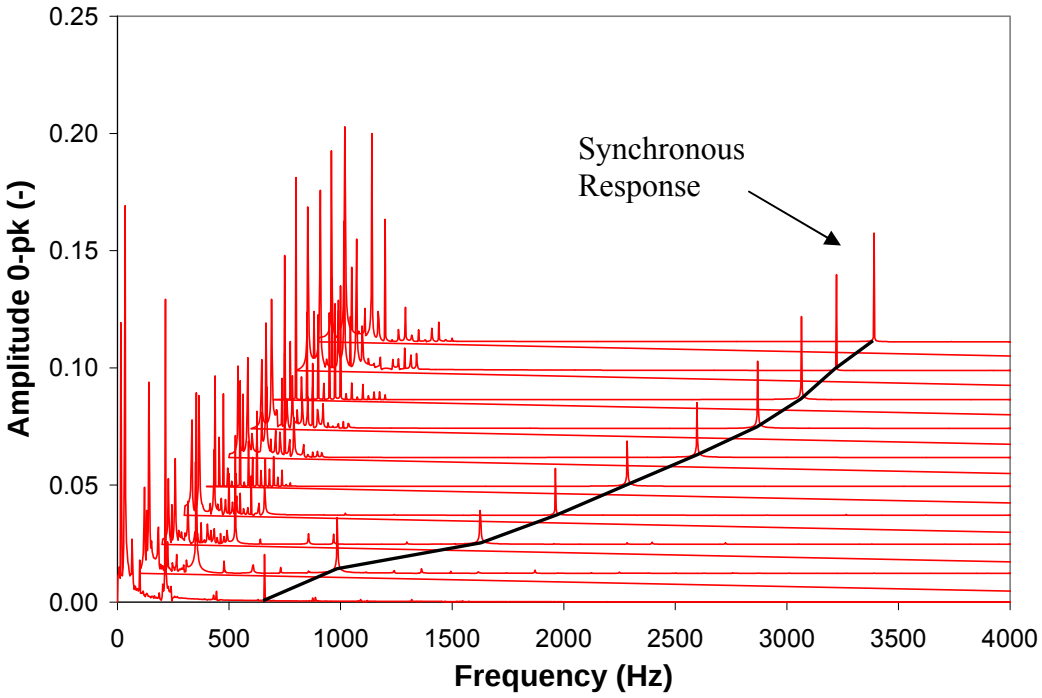

Figure A.1 Predicted waterfall of shaft motion relative to compressor housing with housing accelerations for 50% engine load. Motion is at compressor nose along vertical direction

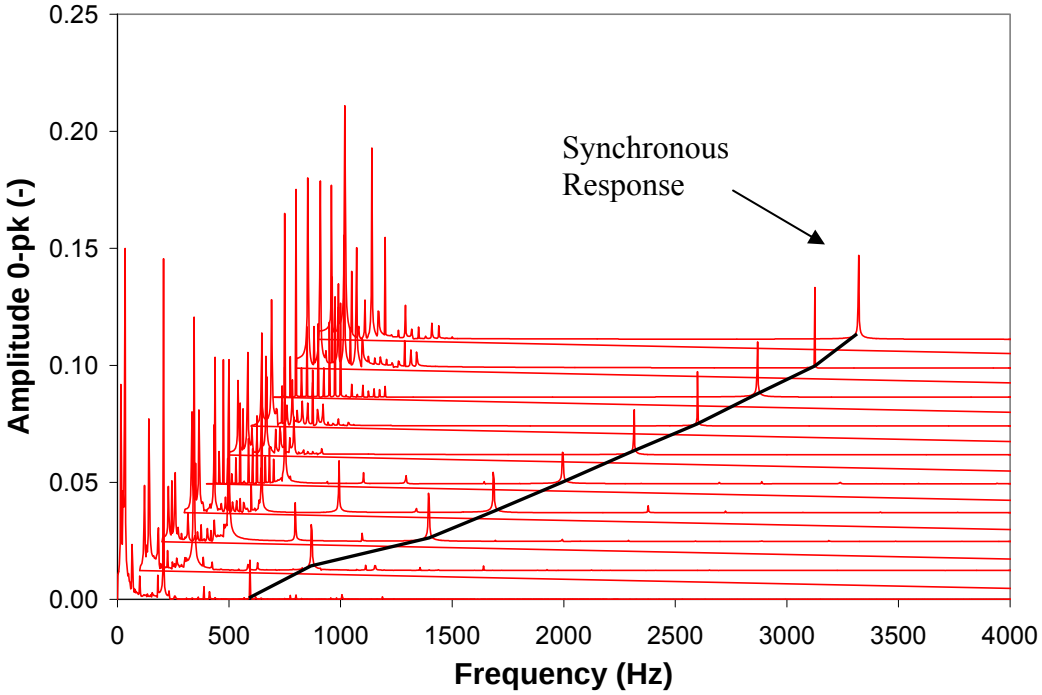

Figure A.2 Predicted waterfall of shaft motion relative to compressor housing with housing accelerations for 25% engine load. Motion is at compressor nose along vertical direction

APPENDIX B CENTER HOUSING AND COMPRESSOR HOUSING INPUT INTO ROTORDYNAMICS MODEL

Table B.1 Center housing acceleration input into rotordynamics model. 100% engine load

Condition #01						Condition #02					
Engine Speed =	3,599	rpm				Engine Speed =	3,249	rpm			
Turbine Speed =	157,647	rpm				Turbine Speed =	152,532	rpm			
Freq. Order	Frequency	Accel - X	Accel - Y	Phase - X	Phase - Y	Freq. Order	Frequency	Accel - X	Accel - Y	Phase - X	Phase - Y
--	[Hz]	[m/s^2]	[m/s^2]	[deg]	[deg]	--	[Hz]	[m/s^2]	[m/s^2]	[deg]	[deg]
1	60	2.5	2.8	20	-128	1	54	0.9	3.0	-103	-157
1.5	90	1.1	4.1	79	172	1.5	81	0.8	1.8	-26	149
2	120	16.6	20.9	7	-164	2	108	8.7	14.1	-134	47
2.5	150	14.0	6.1	-105	66	2.5	135	6.0	1.5	-120	-53
3	180	11.0	2.3	-111	77	3	162	21.4	18.6	43	177
3.5	210	26.4	8.8	-113	76	3.5	190	17.3	13.6	-151	31
4	240	161.9	87.6	36	-21	4	217	102.7	54.8	124	-50
4.5	270	4.7	16.2	113	-89	4.5	244	27.0	12.7	-119	86
5	300	19.2	57.1	72	137	5	271	50.7	86.6	126	-79
5.5	330	4.5	1.9	-39	47	5.5	298	10.8	21.9	-34	97
6	360	16.2	6.9	165	-61	6	325	19.8	6.4	-75	-174
6.5	390	25.1	23.1	91	-17	6.5	352	6.5	7.3	148	155
7	420	12.9	13.8	3	-57	7	379	20.5	12.9	-108	83
7.5	450	14.7	15.7	92	179	7.5	406	8.0	7.3	-126	46
8	480	10.6	11.2	132	9	8	433	12.7	15.6	-107	56
8.5	510	18.8	30.9	158	-72	8.5	460	14.1	10.0	118	-104
9	540	5.7	37.7	-14	148	9	487	31.1	32.9	123	-112
9.5	570	22.0	9.0	166	20	9.5	514	16.5	28.6	68	-139
10	600	5.1	5.9	53	-109	10	542	2.6	26.0	43	-79

Table B.1 continued

Condition #03						Condition #04					
Engine Speed =	3,000	rpm				Engine Speed =	2,751	rpm			
Turbine Speed =	148,722	rpm				Turbine Speed =	146,106	rpm			
Freq. Order	Frequency	Accel - X	Accel - Y	Phase - X	Phase - Y	Freq. Order	Frequency	Accel - X	Accel - Y	Phase - X	Phase – Y
--	[Hz]	[m/s^2]	[m/s^2]	[deg]	[deg]	--	[Hz]	[m/s^2]	[m/s^2]	[deg]	[deg]
1	50	1.3	1.8	176	-39	1	46	1.0	0.9	82	-94
1.5	75	0.2	1.5	80	-35	1.5	69	0.4	0.7	-95	86
2	100	9.4	12.2	110	-81	2	92	8.6	11.2	-119	42
2.5	125	2.7	2.3	-65	-169	2.5	115	1.2	1.4	-59	-51
3	150	12.9	11.9	-94	56	3	138	7.0	5.9	-75	63
3.5	175	9.2	4.0	177	-39	3.5	160	12.2	5.8	146	-81
4	200	45.6	24.1	-126	60	4	183	40.0	12.8	110	-62
4.5	225	11.0	6.9	179	-42	4.5	206	13.0	4.3	28	-168
5	250	35.1	33.5	-164	-69	5	229	22.1	15.3	76	114
5.5	275	24.4	43.1	-179	-27	5.5	252	18.0	14.8	-80	-75
6	300	24.5	57.4	-146	-167	6	275	19.3	26.6	-97	89
6.5	325	0.9	4.5	-99	70	6.5	298	4.5	16.9	161	-67
7	350	14.8	13.3	97	122	7	321	9.9	16.4	-64	-5
7.5	375	3.1	1.9	45	-142	7.5	344	0.5	3.3	81	75
8	400	14.2	12.7	171	-84	8	367	4.5	0.7	-140	-19
8.5	425	4.2	5.1	15	-126	8.5	390	2.4	3.1	60	-43
9	450	11.4	12.0	87	136	9	413	12.7	12.3	-143	156
9.5	475	11.0	10.8	148	-67	9.5	435	5.1	5.5	45	-86
10	500	0.1	3.2	132	-5	10	458	2.0	1.8	-86	20

Table B.1 continued

Condition #05						Condition #06					
Engine Speed =	2,501	rpm				Engine Speed =	2,251	rpm			
Turbine Speed =	144,036	rpm				Turbine Speed =	141,762	rpm			
Freq. Order	Frequency	Accel - X	Accel - Y	Phase - X	Phase - Y	Freq. Order	Frequency	Accel - X	Accel - Y	Phase - X	Phase - Y
--	[Hz]	[m/s^2]	[m/s^2]	[deg]	[deg]	--	[Hz]	[m/s^2]	[m/s^2]	[deg]	[deg]
1	42	0.7	0.8	-137	51	1	38	0.8	0.7	151	-34
1.5	63	0.8	1.0	-71	84	1.5	56	0.7	0.9	72	-110
2	83	15.2	4.8	-171	-29	2	75	16.8	4.0	-27	111
2.5	104	1.2	1.1	133	-154	2.5	94	0.4	1.5	-90	96
3	125	2.9	2.0	23	166	3	113	0.8	0.5	35	178
3.5	146	3.5	6.7	154	-97	3.5	131	2.3	2.0	-30	-178
4	167	48.8	32.7	-34	140	4	150	33.6	15.6	-106	77
4.5	188	11.5	8.5	173	33	4.5	169	6.3	2.6	43	107
5	208	10.4	9.7	155	66	5	188	5.0	13.5	93	-37
5.5	229	14.2	9.1	-105	-54	5.5	206	6.2	6.8	-153	40
6	250	65.3	45.2	29	0	6	225	36.5	30.2	88	-133
6.5	271	7.5	15.8	-138	21	6.5	244	6.8	5.9	-180	-17
7	292	13.3	44.6	-37	62	7	263	13.5	10.3	-23	-133
7.5	313	4.0	2.1	28	20	7.5	281	7.2	14.2	63	-152
8	333	5.2	5.4	147	19	8	300	5.6	13.5	-87	-106
8.5	354	5.3	3.5	-41	-22	8.5	319	1.4	2.2	139	172
9	375	7.1	3.8	166	-47	9	338	4.9	6.6	48	91
9.5	396	10.4	9.9	-179	-66	9.5	356	3.5	2.9	-59	16
10	417	5.4	6.3	-5	126	10	375	6.6	5.6	172	8

Table B.1 continued

Condition #07						Condition #08					
Engine Speed =	2,000	rpm				Engine Speed =	1,749	rpm			
Turbine Speed =	134,298	rpm				Turbine Speed =	120,216	rpm			
Freq. Order	Frequency	Accel - X	Accel - Y	Phase - X	Phase - Y	Freq. Order	Frequency	Accel - X	Accel - Y	Phase - X	Phase - Y
--	[Hz]	[m/s^2]	[m/s^2]	[deg]	[deg]	--	[Hz]	[m/s^2]	[m/s^2]	[deg]	[deg]
1	33	0.5	0.6	107	-80	1	29	0.4	0.3	-16	90
1.5	50	0.5	0.8	7	-177	1.5	44	0.6	0.5	-19	-170
2	67	21.1	5.3	-96	48	2	58	24.4	2.9	-107	33
2.5	83	0.9	0.8	174	-29	2.5	73	0.5	0.5	144	-60
3	100	0.1	0.9	-127	72	3	87	0.3	0.5	-42	168
3.5	117	0.3	0.6	-148	38	3.5	102	0.4	0.4	169	50
4	133	24.6	10.0	98	-74	4	117	19.6	5.9	48	-130
4.5	150	6.0	1.1	-84	14	4.5	131	1.8	0.6	169	-179
5	167	5.8	4.1	-49	144	5	146	1.2	2.2	-166	-39
5.5	183	4.2	3.9	59	-94	5.5	160	2.7	1.1	160	-51
6	200	22.4	9.8	-106	65	6	175	13.7	6.7	179	-3
6.5	217	7.7	4.4	-21	138	6.5	190	2.5	2.1	-164	50
7	233	16.0	8.2	-176	-85	7	204	2.4	6.8	73	-36
7.5	250	12.4	8.1	-173	-128	7.5	219	5.5	3.2	-42	-29
8	267	4.1	1.5	43	-117	8	233	23.7	9.1	-50	128
8.5	283	3.8	5.1	-22	152	8.5	248	8.4	5.5	-101	10
9	300	3.7	11.6	172	-119	9	262	6.6	4.4	-80	17
9.5	317	2.7	4.2	126	176	9.5	277	0.7	1.2	-9	-164
10	333	9.0	9.2	139	103	10	292	1.1	8.3	110	-21

Table B.1 continued

Condition #09						Condition #10					
Engine Speed =	1,249	rpm				Engine Speed =	1,001	rpm			
Turbine Speed =	69,366	rpm				Turbine Speed =	48,504	rpm			
Freq. Order	Frequency	Accel - X	Accel - Y	Phase - X	Phase - Y	Freq. Order	Frequency	Accel - X	Accel - Y	Phase - X	Phase - Y
--	[Hz]	[m/s^2]	[m/s^2]	[deg]	[deg]	--	[Hz]	[m/s^2]	[m/s^2]	[deg]	[deg]
1	21	0.5	0.2	-117	88	1	17	0.2	0.5	82	-45
1.5	31	0.6	0.3	-55	118	1.5	25	0.4	0.2	-124	-32
2	42	21.4	2.8	-157	-18	2	33	24.1	3.4	150	-54
2.5	52	0.6	0.2	98	-90	2.5	42	0.5	0.0	63	-152
3	62	0.3	0.2	30	-89	3	50	0.1	0.1	87	16
3.5	73	0.4	0.2	72	-108	3.5	58	0.0	0.1	27	-161
4	83	12.5	2.9	-72	120	4	67	11.2	2.1	158	-12
4.5	94	0.8	0.3	147	56	4.5	75	0.3	0.1	65	-129
5	104	0.5	0.4	34	-19	5	83	0.1	0.2	41	-14
5.5	115	0.1	0.1	174	-23	5.5	92	0.0	0.1	76	-118
6	125	7.6	2.4	16	-155	6	100	4.2	1.7	178	0
6.5	135	1.3	0.2	-171	-19	6.5	108	0.1	0.1	173	-62
7	146	0.3	1.0	121	58	7	117	0.3	0.4	42	29
7.5	156	0.5	0.4	-42	112	7.5	125	0.2	0.2	95	-57
8	167	10.1	4.0	93	-78	8	133	1.7	0.6	-157	16
8.5	177	1.0	0.9	-155	25	8.5	142	0.3	0.2	-115	-10
9	187	2.0	1.9	-168	126	9	150	0.2	0.4	-101	29
9.5	198	1.2	1.2	-41	156	9.5	159	0.4	0.2	-167	-168
10	208	3.9	3.5	167	-21	10	167	3.6	1.0	-154	35

Table B.2 Compressor housing acceleration input into rotordynamics model. 100% engine load

Condition #01						Condition #02					
Engine Speed =	3,599	rpm				Engine Speed =	3,249	rpm			
Turbine Speed =	157,647	rpm				Turbine Speed =	152,532	rpm			
Freq. Order	Frequency	Accel - X	Accel - Y	Phase - X	Phase - Y	Freq. Order	Frequency	Accel - X	Accel - Y	Phase - X	Phase - Y
--	[Hz]	[m/s^2]	[m/s^2]	[deg]	[deg]	--	[Hz]	[m/s^2]	[m/s^2]	[deg]	[deg]
1	60	2.5	2.8	-24	-44	1	54	0.9	3.0	-108	-123
1.5	90	1.1	4.1	129	159	1.5	81	0.8	1.8	169	165
2	120	16.6	20.9	-5	163	2	108	8.7	14.1	-158	11
2.5	150	14.0	6.1	-115	-49	2.5	135	6.0	1.5	-131	-48
3	180	11.0	2.3	-126	83	3	162	21.4	18.6	32	150
3.5	210	26.4	8.8	-143	119	3.5	190	17.3	13.6	-178	67
4	240	161.9	87.6	-4	140	4	217	102.7	54.8	111	-103
4.5	270	4.7	16.2	100	-88	4.5	244	27.0	12.7	180	-21
5	300	19.2	57.1	88	164	5	271	50.7	86.6	121	-90
5.5	330	4.5	1.9	-140	74	5.5	298	10.8	21.9	-62	66
6	360	16.2	6.9	-88	40	6	325	19.8	6.4	-174	-86
6.5	390	25.1	23.1	72	-137	6.5	352	6.5	7.3	82	177
7	420	12.9	13.8	54	-136	7	379	20.5	12.9	-170	-26
7.5	450	14.7	15.7	137	-72	7.5	406	8.0	7.3	88	-145
8	480	10.6	11.2	3	159	8	433	12.7	15.6	-58	99
8.5	510	18.8	30.9	-96	61	8.5	460	14.1	10.0	-111	47
9	540	5.7	37.7	63	160	9	487	31.1	32.9	-108	61
9.5	570	22.0	9.0	19	159	9.5	514	16.5	28.6	-136	24
10	600	5.1	5.9	-135	81	10	542	2.6	26.0	-108	-94

Table B.2 continued

Condition #03						Condition #04					
Engine Speed =	3,000	rpm				Engine Speed =	2,751	rpm			
Turbine Speed =	148,722	rpm				Turbine Speed =	146,106	rpm			
Freq. Order	Frequency	Accel - X	Accel - Y	Phase - X	Phase - Y	Freq. Order	Frequency	Accel - X	Accel - Y	Phase - X	Phase - Y
--	[Hz]	[m/s^2]	[m/s^2]	[deg]	[deg]	--	[Hz]	[m/s^2]	[m/s^2]	[deg]	[deg]
1	50	1.3	1.8	168	-98	1	46	1.0	0.9	73	42
1.5	75	0.2	1.5	0	-95	1.5	69	0.4	0.7	-118	60
2	100	9.4	12.2	117	-89	2	92	8.6	11.2	-120	79
2.5	125	2.7	2.3	-82	141	2.5	115	1.2	1.4	-56	-142
3	150	12.9	11.9	-107	-2	3	138	7.0	5.9	-77	35
3.5	175	9.2	4.0	152	148	3.5	160	12.2	5.8	136	-84
4	200	45.6	24.1	-137	6	4	183	40.0	12.8	97	-172
4.5	225	11.0	6.9	152	-72	4.5	206	13.0	4.3	0	-127
5	250	35.1	33.5	-118	-19	5	229	22.1	15.3	78	125
5.5	275	24.4	43.1	173	-36	5.5	252	18.0	14.8	-110	22
6	300	24.5	57.4	162	-134	6	275	19.3	26.6	-159	-23
6.5	325	0.9	4.5	-162	-80	6.5	298	4.5	16.9	124	-70
7	350	14.8	13.3	121	-145	7	321	9.9	16.4	-9	42
7.5	375	3.1	1.9	-67	70	7.5	344	0.5	3.3	47	148
8	400	14.2	12.7	-146	-4	8	367	4.5	0.7	-28	32
8.5	425	4.2	5.1	-22	-172	8.5	390	2.4	3.1	32	-145
9	450	11.4	12.0	118	-87	9	413	12.7	12.3	-101	51
9.5	475	11.0	10.8	-57	119	9.5	435	5.1	5.5	19	-170
10	500	0.1	3.2	-153	5	10	458	2.0	1.8	83	-177

Table B.2 continued

Condition #05						Condition #06					
Engine Speed =	2,501	rpm				Engine Speed =	2,251	rpm			
Turbine Speed =	144,036	rpm				Turbine Speed =	141,762	rpm			
Freq. Order	Frequency	Accel - X	Accel - Y	Phase - X	Phase - Y	Freq. Order	Frequency	Accel - X	Accel - Y	Phase - X	Phase - Y
--	[Hz]	[m/s^2]	[m/s^2]	[deg]	[deg]	--	[Hz]	[m/s^2]	[m/s^2]	[deg]	[deg]
1	42	0.7	0.8	-136	-157	1	38	0.8	0.7	151	89
1.5	63	0.8	1.0	-38	103	1.5	56	0.7	0.9	83	-108
2	83	15.2	4.8	-159	-24	2	75	16.8	4.0	-18	133
2.5	104	1.2	1.1	116	60	2.5	94	0.4	1.5	-73	110
3	125	2.9	2.0	20	132	3	113	0.8	0.5	35	134
3.5	146	3.5	6.7	-178	-73	3.5	131	2.3	2.0	-60	-53
4	167	48.8	32.7	-67	70	4	150	33.6	15.6	-112	25
4.5	188	11.5	8.5	140	75	4.5	169	6.3	2.6	-3	34
5	208	10.4	9.7	93	126	5	188	5.0	13.5	23	-45
5.5	229	14.2	9.1	-76	-18	5.5	206	6.2	6.8	164	91
6	250	65.3	45.2	-42	90	6	225	36.5	30.2	68	-157
6.5	271	7.5	15.8	-102	71	6.5	244	6.8	5.9	136	-49
7	292	13.3	44.6	-41	80	7	263	13.5	10.3	-56	96
7.5	313	4.0	2.1	90	49	7.5	281	7.2	14.2	43	-158
8	333	5.2	5.4	61	129	8	300	5.6	13.5	-133	-75
8.5	354	5.3	3.5	-60	22	8.5	319	1.4	2.2	-122	-81
9	375	7.1	3.8	-42	70	9	338	4.9	6.6	63	153
9.5	396	10.4	9.9	-121	15	9.5	356	3.5	2.9	-42	58
10	417	5.4	6.3	99	-143	10	375	6.6	5.6	-158	-11

Table B.2 continued

Condition #07						Condition #08					
Engine Speed =	2,000	rpm				Engine Speed =	1,749	rpm			
Turbine Speed =	134,298	rpm				Turbine Speed =	120,216	rpm			
Freq. Order	Frequency	Accel - X	Accel - Y	Phase - X	Phase - Y	Freq. Order	Frequency	Accel - X	Accel - Y	Phase - X	Phase - Y
--	[Hz]	[m/s^2]	[m/s^2]	[deg]	[deg]	--	[Hz]	[m/s^2]	[m/s^2]	[deg]	[deg]
1	33	0.5	0.6	100	65	1	29	0.4	0.3	-20	-106
1.5	50	0.5	0.8	7	-132	1.5	44	0.6	0.5	-27	-81
2	67	21.1	5.3	-96	86	2	58	24.4	2.9	-108	97
2.5	83	0.9	0.8	177	65	2.5	73	0.5	0.5	140	-35
3	100	0.1	0.9	-95	72	3	87	0.3	0.5	-62	-133
3.5	117	0.3	0.6	-162	121	3.5	102	0.4	0.4	156	-148
4	133	24.6	10.0	91	-106	4	117	19.6	5.9	46	-156
4.5	150	6.0	1.1	-100	-47	4.5	131	1.8	0.6	152	88
5	167	5.8	4.1	-79	132	5	146	1.2	2.2	-140	-49
5.5	183	4.2	3.9	17	-50	5.5	160	2.7	1.1	145	-52
6	200	22.4	9.8	-109	25	6	175	13.7	6.7	156	-46
6.5	217	7.7	4.4	-38	123	6.5	190	2.5	2.1	165	76
7	233	16.0	8.2	-178	-79	7	204	2.4	6.8	66	9
7.5	250	12.4	8.1	175	-79	7.5	219	5.5	3.2	-43	22
8	267	4.1	1.5	-97	131	8	233	23.7	9.1	-63	67
8.5	283	3.8	5.1	-27	107	8.5	248	8.4	5.5	-112	13
9	300	3.7	11.6	-178	-70	9	262	6.6	4.4	-65	73
9.5	317	2.7	4.2	-165	-118	9.5	277	0.7	1.2	-97	73
10	333	9.0	9.2	74	-171	10	292	1.1	8.3	-156	37

Table B.2 continued

Condition #09						Condition #10					
Engine Speed =	1,249	rpm				Engine Speed =	1,001	rpm			
Turbine Speed =	69,366	rpm				Turbine Speed =	48,504	rpm			
Freq. Order	Frequency	Accel - X	Accel - Y	Phase - X	Phase - Y	Freq. Order	Frequency	Accel - X	Accel - Y	Phase - X	Phase - Y
--	[Hz]	[m/s^2]	[m/s^2]	[deg]	[deg]	--	[Hz]	[m/s^2]	[m/s^2]	[deg]	[deg]
1	21	0.5	0.2	-124	97	1	17	0.2	0.5	61	-72
1.5	31	0.6	0.3	-58	161	1.5	25	0.4	0.2	-126	174
2	42	21.4	2.8	-156	71	2	33	24.1	3.4	151	-5
2.5	52	0.6	0.2	98	-43	2.5	42	0.5	0.0	69	-138
3	62	0.3	0.2	-10	10	3	50	0.1	0.1	52	92
3.5	73	0.4	0.2	67	-82	3.5	58	0.0	0.1	103	-65
4	83	12.5	2.9	-77	114	4	67	11.2	2.1	156	-19
4.5	94	0.8	0.3	141	76	4.5	75	0.3	0.1	65	-164
5	104	0.5	0.4	23	28	5	83	0.1	0.2	49	34
5.5	115	0.1	0.1	-170	74	5.5	92	0.0	0.1	145	-112
6	125	7.6	2.4	8	175	6	100	4.2	1.7	173	-30
6.5	135	1.3	0.2	178	12	6.5	108	0.1	0.1	-93	-121
7	146	0.3	1.0	100	68	7	117	0.3	0.4	39	40
7.5	156	0.5	0.4	-63	174	7.5	125	0.2	0.2	98	33
8	167	10.1	4.0	76	-116	8	133	1.7	0.6	-158	-92
8.5	177	1.0	0.9	168	93	8.5	142	0.3	0.2	-122	73
9	187	2.0	1.9	147	135	9	150	0.2	0.4	-99	22
9.5	198	1.2	1.2	-121	-172	9.5	159	0.4	0.2	-175	84
10	208	3.9	3.5	167	-62	10	167	3.6	1.0	-169	-3

VITA

Ashley Maruyama received his Bachelor of Science degree in chemical engineering from Texas A&M University in 2004. In 2005, he entered the mechanical engineering graduate program at Texas A&M University and began work at the Texas A&M Turbomachinery Laboratory. He received his Master of Science degree on December 14, 2007. His research interests include rotordynamics and computer modeling of various turbomachinery. Currently, he is employed by Sulzer Turbo Services as a technical programmer.

Mr. Maruyama may be reached at Sulzer-Hickham, Inc., 11518 Old LaPorte Road, LaPorte, Texas, 77571. His email address is ash.maruyama@gmail.com.